ARTICLE

Check for updates

Convergent mitochondrial impairment and apoptosis driven by simultaneous down-regulation of multiple genes at 11p11.2 in Alzheimer's disease

Jinsong Yu[1,2], Min Xu[1,2], Xiao-rong Wu[1,2], Wei-Bo Kang[1,2], Wei-Yin Zou[1,2], Qianjin Liu[1,2], Deng-Feng Zhang[1,2] and Yong-Gang Yao[1,2,3]✉

Genome-wide association studies (GWAS) and multi-omics analyses have identified numerous risk loci and thousands of potential causal genes associated with Alzheimer's disease (AD). However, the synergistic pathogenic contributions of multiple low-risk causal genes within a single locus remain poorly understood. Polygenic synergism at the 11p11.2 locus was systematically examined in AD pathogenesis. Three causal genes (*MTCH2*, *NDUFS3*, and *PSMC3*) exhibited coordinated down-regulation in both AD patients and AD mouse models. Individual knockdown in cultured cells altered mitochondrial function and disrupted AD-associated pathways, as revealed by transcriptomic profiling. Integrated RNA-seq analysis and experimental validation demonstrated that the concurrent down-regulation of all three genes synergistically enhanced mitochondrial reactive oxygen species (ROS) generation and activated the caspase-7-mediated apoptotic pathway. Notably, pharmacological caspase inhibition with Q-VD-OPh attenuated neuronal apoptosis, ameliorated memory deficits, and reduced Aβ plaque deposition in APP/PS1 mice. Simultaneous down-regulation of multiple genes at the 11p11.2 locus contributed to mitochondrial dysfunction and apoptosis in AD, highlighting polygenic synergism as a key pathogenic mechanism.

Molecular Psychiatry; https://doi.org/10.1038/s41380-026-03664-7

BACKGROUND

Alzheimer's disease (AD) is a progressive neurodegenerative disorder characterized by a gradual decline in memory and cognitive function [1, 2]. Despite extensive research, the therapeutic landscape for AD remains largely ineffective, primarily due to the complex disease etiology and the absence of well-defined molecular targets [2]. While aging is the primary risk factor for this neurodegenerative condition, genetic predisposition also plays a significant role [3, 4]. Large-scale genome-wide association studies (GWAS) and multi-omics analyses have identified numerous risk loci and thousands of potential susceptibility genes, underscoring the polygenic nature of the disease [5–9]. Mutations in Aβ precursor protein (*APP*), presenilin-1 (*PSEN1*), and presenilin-2 (*PSEN2*) have been established as the primary drivers of early-onset AD, accounting for approximately 5% of cases [4, 10–12]. In contrast, the genetic architecture of late-onset AD, which affects the vast majority of patients, results from a network of weakly penetrant genetic variants that collectively contribute to disease progression. Rather than being driven by single pathogenic mutations and genes, late-onset AD arises from interactions among multiple susceptibility genes and regulatory elements, necessitating a deeper understanding of their combined effects [4, 5].

Our recent functional genomic study of the 11p11.2 locus identified 24 potential functional variants (fVars) and six target genes (*MTCH2*, *ACP2*, *NDUFS3*, *PSMC3*, *C1QTNF4*, and *MADD*, ranked by convergent functional genomics score) potentially involved in AD pathogenesis [13]. These findings suggest that multiple variants and genes at 11p11.2 may collectively contribute to AD risk. This pattern of polygenic interaction within a single locus has been observed in other neurological disorders, such as schizophrenia [14, 15], where multiple risk genes within a single locus exert synergistic effects on disease susceptibility. While the concept of multigene contribution in AD has been proposed, direct experimental validation remains limited. In this study, we investigated the cooperative effects of multiple causal genes at 11p11.2 using a multigene synergy analysis framework [16]. Results demonstrated that *MTCH2*, *NDUFS3*, and *PSMC3* at 11p11.2 were consistently down-regulated in both AD patients and AD mouse models. Functional analyses revealed that their simultaneous reduction amplified mitochondrial dysfunction, increased reactive oxygen species (ROS) production, and promoted apoptotic signaling, collectively exacerbating AD pathology. Furthermore, pharmacological inhibition of apoptosis ameliorated memory impairment, reduced amyloid burden, and decreased neuronal loss in APP/PS1 mice. These results establish a mechanistic model in which polygenic synergism at

[1]State Key Laboratory of Genetic Evolution and Animal Models, Yunnan Key Laboratory of Animal Models and Human Disease Mechanisms, and KIZ-CUHK Joint Laboratory of Bioresources and Molecular Research in Common Diseases, Kunming Institute of Zoology, Chinese Academy of Sciences, Kunming, Yunnan 650204, China. [2]National Research Facility for Phenotypic & Genetic Analysis of Model Animals (Primate Facility), National Resource Center for Non-Human Primates, Yunnan Engineering Center on Brain Disease Models, Kunming Institute of Zoology, Chinese Academy of Sciences, Kunming 650107, China. [3]Kunming College of Life Science, University of Chinese Academy of Sciences, Kunming, Yunnan 650204, China. ✉email: yaoyg@mail.kiz.ac.cn

Received: 25 April 2025 Revised: 22 April 2026 Accepted: 20 May 2026
Published online: 28 May 2026

11p11.2 contributes to AD pathogenesis, providing new insights into the molecular basis of neurodegeneration.

MATERIALS AND METHODS

Mice

All APP/PS1 (APP/PSEN1△E9) and wild-type (WT) mice (male, 5–8 months old) were housed under a 12 h light/dark cycle at a temperature of 22–25 °C. APP/PSEN1 mice, which overexpress mutated human *APP* (Swedish mutations K595N/M596L) and human *PSEN1* (presenilin 1) deleted from exon 9 [17, 18], were originally obtained from the Jackson Laboratory (stock no. #34829-JAX, Bar Harbor, ME, USA). The genotypes of mice were determined by polymerase chain reaction (PCR) analysis of DNA extracted from mouse toes using primer pairs 5′-GACTGACCACTCGAC CAGGTTCTG-3′ / 5′-CTTGTAAGTTGGATTCTCATATCCG-3′ and 5′-AATAGAGA ACGGCAGGAGCA-3′ / 5′-GCCATGAGGGCACTAATCAT-3′ for *APP* and *PSEN1*, respectively. All experiments were performed using male mice with random group assignment (detailed in the figure legends). All animal experiments were approved by the Institutional Animal Care and Use Committee of Kunming Institute of Zoology, Chinese Academy of Sciences.

Cell line

The SH-SY5Y and HEK293T cell lines were obtained from the Kunming Cell Bank at Kunming Institute of Zoology, Chinese Academy of Sciences. The U251-APP cell line, which stably expresses the APP mutant p.M671L, was established in our previous study [19]. The cell lines were cultured at 37 °C in Dulbecco's modified Eagle's medium (DMEM, Gibco, USA) supplemented with 10% fetal bovine serum and 1% penicillin/streptomycin (Thermo Fisher, USA).

Stereo-seq analysis

Stereo-seq spatial transcriptomics technology [20] was applied to profile brain sections from one APP/PS1 mouse and one WT mouse, with sequencing performed at Yucebio (Shenzhen, China). Raw sequencing data were aligned and quantified using the Stereo-seq Analysis Workflow (SAW) pipeline, yielding a gene expression matrix at the spot level. To enhance spatial resolution, spots were aggregated into a bin50 expression matrix, improving gene expression signal strength at each spatial location. Based on nuclear staining images, cell segmentation was performed, assigning expression data to individual cells and generating a cell-level expression matrix, as previously described [20].

For downstream data analysis, stereopy (https://github.com/STOmics/stereopy) and scanpy [21] were used for quality control and clustering. Spatial clustering analysis was conducted using the bin50 expression matrix, and clusters were annotated into nine common brain regions with reference to the Allen Brain Atlas (https://atlas.brain-map.org/). To further refine cell-type annotation, the MapMyCells mouse brain cell atlas (https://knowledge.brain-map.org/mapmycells/process) was employed, enabling hierarchical mapping of the cell-bin-level expression matrix and the construction of a spatial atlas of mouse brain cells [22].

For the genes of interest, we calculated Pearson correlation coefficients and corresponding statistical significance (via *t*-test) across the thousands of cellbins within each animal. Correlations with $P < 0.05$ were considered significant, and corresponding heatmaps were generated to visualize the relationships among genes.

Immunofluorescence

Mice were anesthetized with isoflurane, and major organs, including the heart, liver, spleen, lungs, kidneys, and brain, were excised, weighed, and fixed in 4% paraformaldehyde (PFA)/phosphate-buffered saline (PBS) at 4 °C. Tissues were incubated overnight in 30% sucrose/PBS at 4 °C, followed by sectioning into 15-μm slices using a freezing microtome (RWD, Minux FS800). Brain sections were blocked in a solution containing 5% bovine serum albumin (BSA) and 0.1% Triton X-100 in PBS at room temperature for 1 h, followed by overnight incubation at 4 °C with the indicated primary antibodies (rabbit anti-NeuN, 1:500, EMD Millipore, ABN78; mouse anti-4G8, 1:500, BioLegend, SIG-39220). After four washes with PBS (5 min each) at room temperature, sections were incubated with the secondary antibodies (anti-mouse, 1:1000, Jackson ImmunoResearch, 115-545-003; anti-rabbit, 1:1000, Jackson ImmunoResearch, 711-295-152) and 4′,6-diamidino-2-phenylindole (DAPI, Meilunbio, MB3204) in blocking buffer for 2 h at 37 °C, respectively. After another four washes with PBS at room temperature, images were captured using confocal microscopy (TissueGnostics or Olympus SpinSR10), with image analysis performed using ImageJ [23] or TissueGnostics analysis software.

RNA interference and transfection

Small interfering RNAs (siRNAs) targeting *MTCH2*, *ACP2*, *NDUFS3*, and *PSMC3*, along with a negative control (NC) siRNA, were purchased from RiboBio (Table S1, Guangzhou, China). For gene knockdown experiments in U251-APP cells, cells were seeded in 6-well plates at a density of 2×10^5 per well and grown to approximately 70% confluence before transfection. Transfection was performed using 20 nM siRNA and Lipofectamine™ 3000, following the manufacturer's standard protocols.

For the knockdown of multiple genes, we used same concentration of total siRNAs across all experimental groups to ensure comparable cellular stress induced by siRNA delivery. Briefly, control group, 60 nM siNC; MTCH2_KD group, 20 nM siMTCH2 + 40 nM siNC; NDUFS3_KD group, 20 nM siNDUFS3 + 40 nM siNC; PSMC3_KD group, 20 nM siPSMC3 + 40 nM siNC; M2N3_KD group, 20 nM siMTCH2 + 20 nM siNDUFS3 + 20 nM siNC; M2P3_KD group, 20 nM siMTCH2 + 20 nM siPSMC3 + 20 nM siNC; N3P3_KD group, 20 nM siNDUFS3 + 20 nM siPSMC3 + 20 nM siNC; M2N3P3_KD group (triple gene knockdown group), 20 nM siMTCH2 + 20 nM siNDUFS3 + 20 nM siPSMC3.

To assess $A\beta_{1\text{-}42}$ and phosphorylated Tau (pTau-396) levels, transfected cells were incubated for 24 h before replacing the medium with fresh growth medium containing 1 μg/mL doxycycline (Sigma, D9891) to induce *APP* expression. After 48 h of doxycycline induction, culture supernatants were collected for $A\beta_{1\text{-}42}$ quantification, while cell lysates were used to measure pTau-396 levels by enzyme-linked immunosorbent assay (ELISA). Measurements were performed at 72 h post-transfection.

Western blot analysis

Western blotting was performed following established procedures from previous studies [13, 17, 24]. In brief, cells and tissues were lysed in ice-cold lysis buffer (Beyotime, P0013), and lysates were centrifuged at 12 000 × *g* for 10 min at 4 °C. The supernatant was collected, and total protein concentrations were determined using a BCA Protein Assay Kit (Beyotime, P0012). Equal amounts of protein (20 μg) were resolved by 12% sodium dodecyl sulfate-polyacrylamide gel electrophoresis (SDS-PAGE) and subsequently transferred to polyvinylidene difluoride (PVDF) membranes (Bio-Rad, L1620177). The membranes were placed in 5% (w/v) skimmed milk at room temperature for 2 h and washed three times (5 min each) with TBST (1× TBS solution containing 0.1% Tween-20). The membranes were then incubated with the primary antibodies (Mouse anti-GAPDH, 1:1000, EnoGene, E12-042-3; Mouse anti-β-Tubulin, 1:1000, EnoGene, E1C601; Rabbit anti-MTCH2, 1:1000, Absin, abs143485; Rabbit anti-NDUFS3, 1:1000, GeneTex, GTX105835; Rabbit anti-PSMC3, 1:1000, Abcam, ab171969; Rabbit anti-MADD, 1:1000, Abcam, ab134117; Rabbit anti-C1QTNF4, 1:1000, Abcam, ab36891; Rabbit anti-ACP2, 1:1000, Boster, A06554; anti-Caspase-7, 1:1000, Cell Signaling Technology, 8438; anti-Caspase-7, 1:1000, proteintech, 85328-1-RR; anti-Caspase-9, 1:1000, Abcam, ab202068; anti-Caspase-3, 1:1000, Cell Signaling Technology, 9664 T) at 4 °C overnight, respectively, washed three times with TBST (5 min each), and incubated with corresponding secondary antibodies for 1 h at room temperature. The membranes were again washed with TBST (three times, each 5 min) at room temperature and visualized using an ECL Western Blot Detection Kit (Millipore, WBKLS0500). Protein bands were captured using a Bio-Rad ChemiDoc™ MP imaging system and analyzed with ImageJ.

Co-immunoprecipitation

For transient transfection and co-immunoprecipitation (Co-IP) assays, HEK293T cells were co-transfected with pairwise combinations of plasmids encoding MTCH2-HA, NDUFS3-Flag, PSMC3-Myc, Vector-HA, Vector-Flag, and Vector-Myc (purchased from iGeneBio). After transfection for 48 h, cells were lysed on ice for 1 h in lysis buffer (Beyotime, P0013). Lysates were collected by centrifugation at 12,000 × *g* for 15 min, and the supernatants were incubated with HA beads (ABMagic, MA103-25), Flag beads (ABMagic, MA101-25), or Myc beads (ABMagic, MA105-25) overnight at 4 °C, according to the indicated tag of each plasmid. The beads were washed five times (5 min each) with lysis buffer, and the bound proteins were eluted by boiling in 2 × SDS loading buffer for 5 min. Eluted proteins were detected following the Co-IP procedure described in our previous study [25].

Apoptosis analysis

Cells were dissociated using 0.25% trypsin, collected by centrifugation at 300 × *g* for 5 min at 4 °C, and resuspended in pre-cooled PBS. Apoptosis was

assessed using an Annexin V-FITC/PI Apoptosis Detection Kit (YEASEN, 40302ES60), following the manufacturer's instructions [26]. Briefly, 2-3 × 10^5 cells were incubated in 100 µL of binding buffer containing 5 µL of Annexin V and 10 µL of propidium iodide (PI) for 15 min at room temperature in the dark. After incubation, 400 µL of binding buffer was added to terminate the reaction, and samples were immediately analyzed using flow cytometry (BD LSRFortessa). Data were analyzed using FlowJo software.

Detection of mitochondrial reactive oxygen species (mROS)

MitoSOX (Thermo Fisher, M3600S) was used to determine mROS levels. In brief, U251-APP cells (2-3 × 10^5 cells/well) were seeded in 6-well plates and incubated with 2.5 µM MitoSOX working solution at 37 °C for 20 min in the dark. Following incubation, cells were washed three times with PBS and subsequently stained with 5 µg/mL Hoechst dye (Beyotime, C1022) for nuclear counterstaining. Fluorescence signals were captured using confocal microscopy (Olympus SpinSR10) or quantified by flow cytometry (BD LSRFortessa). Image and cytometric data were analyzed using OlyVIA and FlowJo software, respectively.

Mitochondrial membrane potential (MMP) measurement

MMP changes were measured by using the JC-1 Mitochondrial Membrane Potential Assay Kit (Beyotime, C2003S) following the manufacturer's protocol. Briefly, U251-APP cells were collected, washed with cold PBS, and stained with JC-1 solution (1:1 mixture of culture medium and staining fluid) for 10 min at 37 °C in the dark. Cells were then washed with staining buffer and analyzed by flow cytometry. In cells with high level of MMP, JC-1 forms J-aggregates in mitochondria that emit red fluorescence; conversely, in cells with diminished MMP, JC-1 remains in the cytoplasm as monomers that produce green fluorescence. MMP was expressed as the red/green population ratio following a previous study [27]. Carbonyl cyanide 3-chlorophenylhydrazone (CCCP), which disrupts mitochondrial integrity and induces complete MMP loss, served as a positive control [27].

RNA sequencing (RNA-seq) data processing

RNA sequencing data were processed using an established bioinformatics pipeline, as reported in our previous studies [24, 28, 29]. The quality of raw paired-end reads was evaluated using FastQC (https://www.bioinformatics.babraham.ac.uk/projects/fastqc/). Adapter sequences and low-quality reads were trimmed using fastp [30]. Filtered reads were aligned to the human (*Homo sapiens*, GRCh38) or mouse (*Mus musculus*, GRCm39) reference genome, obtained from the Ensembl database (https://www.ensembl.org/index.html), using HISAT2 [31] or STAR [32] with default parameters. Gene expression levels were assessed and normalized using StringTie [33] or RSEM [34]. Differentially expressed genes (DEGs) were identified using the DESeq2 package in R, applying a cutoff threshold of $|\text{fold change}| > 1.5$, $P\text{-value} < 0.05$, and adjusted $P\text{-value} < 0.2$. Kyoto Encyclopedia of Genes and Genomes (KEGG) and Gene Ontology (GO) enrichment analyses were performed using the clusterProfiler package in R [35, 36], while data visualization was performed using the ggplot2 package in R [37]. Schematic illustrations were generated using Adobe Illustrator and the Generic Diagramming Platform (GDP) [38].

Analysis of synergistic gene effects

The experimental design and assessment of synergy-driven gene expression were based on established protocols [14–16]. Bulk RNA-seq libraries were generated from U251-APP cells subjected to individual knockdown of *MTCH2* (MTCH2_KD), *NDUFS3* (NDUFS3_KD), and *PSMC3* (PSMC3_KD), as well as combined knockdown of all three genes (MTCH2_KD + NDUFS3_KD + PSMC3_KD (M2N3P3_KD)). Low-expression genes were filtered using a counts per million (CPM) cut-off of 1.25, retaining approximately 13 000 genes for downstream analysis. Linear modeling was performed using a standardized workflow. The *voom()* function was applied to transform raw counts into logCPM values and compute precision weights to adjust for heteroscedasticity. The *lmFit()* function was then used to fit the linear model. The expected additive effect was modeled by summing the individual coefficient comparisons: additive = (MTCH2_KD - CTRL) + (PSMC3_KD – CTRL) + (NDUFS3_KD - CTRL). The synergistic effect was modeled by subtracting the additive effect from the combinatorial perturbation comparison: synergy = (M2N3P3_KD - CTRL) – ((MTCH2_KD - CTRL) + (PSMC3_KD – CTRL) + (NDUFS3_KD - CTRL)).

Differential expression was assessed using the *eBayes()* and *decideTests()* functions, with a false discovery rate (FDR) threshold of 0.1 to determine the synergy coefficient and proportion of DEGs exhibiting synergistic regulation. Functional enrichment analyses, including competitive gene set enrichment analysis (GSEA) and GO over-representation analysis, were performed using the *ids2indices()*, *geneIds()*, and *getGmt()* functions in R, utilizing gene sets from the MSigDB database (https://www.gsea-msigdb.org/gsea/msigdb/collections.jsp). An FDR threshold of 0.1 was applied for GO enrichment analysis to evaluate synergistic effects.

Q-VD-OPh administration in WT and APP/PS1 mice

Quinoline-Val-Asp-difluorophenoxymethylketone (Q-VD-OPh) is a broad-spectrum caspase inhibitor with potent antiapoptotic properties [39, 40]. To evaluate its therapeutic potential, 5-month-old mice were intraperitoneally administered Q-VD-OPh (10 mg/kg, Proteintech, CM03300) or vehicle (saline) every two days for 3 months, following previously established protocols [39]. Behavioral testing was conducted at two time points: 1 month and 3 months after the initiation of Q-VD-OPh treatment. Following the completion of drug administration, mice were anesthetized with isoflurane for tissue collection and further molecular analyses.

Novel object recognition (NOR) test

The NOR task was conducted in three phases: habituation, training, and testing, following a previously established protocol [41]. Twenty-four hours before training, mice were acclimated to an open testing arena (40 × 40 × 40 inches) for 10 min to minimize novelty-induced stress. During the training phase, mice were placed in the same arena containing two identical objects positioned at opposite corners and were allowed to explore freely for 10 min. Memory performance was assessed at two time points: 4 h (short-term memory) and 24 h (long-term memory) after training. In the test session, one of the familiar objects was replaced with a novel object, while the other remained unchanged. Object exploration time was recorded using SMART v3.0 software (Panlab HARVARD, MA, USA), which tracked physical interactions with either object. Recognition memory was quantified using the recognition index (Recognition Index = $T_{novel} / (T_{novel} + T_{familiar})$, where T_{novel} and $T_{familiar}$ represent time spent with the novel and familiar objects, respectively) [41].

Morris water maze (MWM) test

The MWM test was performed according to previously described procedures [24]. During the training phase, a submerged platform was placed in a fixed location, and mice were introduced into the water facing the tank wall from randomly assigned quadrants. Each trial lasted a maximum of 60 s, within which mice were required to locate the platform. If a mouse failed to find the platform within this time, it was gently guided to the platform and allowed to remain there for 15 s before removal. Three trials were conducted daily, with a 2-h interval between each trial. Mice were dried and warmed on a heating pad between trials. Escape latency, defined as the time required to locate the platform, was recorded and averaged for each training day. On day 7, the platform was removed, and a probe trial was conducted to assess spatial memory retention. Mice were released from the quadrant opposite the former platform location, and key behavioral parameters—including the number of platform location crossings, time spent in target quadrant, and swimming speed—were recorded using SMART v3.0 software. All behavioral tests were performed by two investigators who were blinded to the experimental conditions.

Quantitative real-time PCR (qRT-PCR)

Total RNA was extracted from cells and tissues using RNA^{iso} Plus reagent (Takara) following the manufacturer's protocols. Genomic DNA was removed, and reverse transcription was performed using a SynScript$^{@}$III RT SuperMix for qPCR Kit (Tsingke, TSK314S). Relative gene expression was determined using qRT-PCR on a QuantStudio 12 K Flex Real-time PCR system (Thermo Fisher) with SYBR Green Mix (Bio-Rad, #1725124). Target gene expression was normalized to *GAPDH* or *β-actin* mRNA level (as an internal control) in each sample. Primer pairs for qRT-PCR are shown in Table S2.

Enzyme-linked immunosorbent assay (ELISA)

$A\beta_{1\text{-}42}$ (Elabscience, E-EL-H0543c) concentrations in culture supernatants and pTau-396 (Elabscience, E-EL-H5314c) levels in U251-APP cell lysates were respectively analyzed using ELISA kits according to the manufacturer's instructions, as described previously [13]. Briefly, 100 µL of diluted standards, blanks, and samples (in duplicate) were incubated in 96-well plates for 90 min at 37 °C. Following incubation, 100 µL of biotinylated detection antibody working solution was added to each well, followed by

1 h of incubation at 37°C. Wells were then washed three times with wash buffer, and 100 µL of horseradish peroxidase (HRP)-conjugated working solution was added to each well, followed by incubation for 30 min at 37 °C. After washing, 90 µL of substrate reagent was added to each well for 15 min of incubation at 37 °C. The reaction was terminated by adding 50 µL of stop solution per well, and absorbance was measured at 450 nm using a microplate reader (BioTek, Elx808).

Statistical analysis

The data are expressed as mean ± SD unless otherwise stated. Statistical analysis was conducted using GraphPad Prism 8. Two-way unpaired *t*-test, one-way ANOVA, or two-way ANOVA were used. Statistical significance was set at $P < 0.05$. Additional details are provided in the figure legends.

RESULTS

Coordinated down-regulation of multiple genes at the 11p11.2 locus in AD patients and APP/PS1 mice

Our previous functional genomic analyses of the 11p11.2 (CELF1/SPI1) locus identified multiple candidate genes implicated in AD susceptibility [13]. To further characterize their expression patterns across different cell types, single-nucleus RNA sequencing (snRNA-seq) data from AD patients and healthy controls were analyzed [42]. Results revealed that *MTCH2*, *ACP2*, *NDUFS3*, and *PSMC3* were broadly expressed in both neurons and astrocytes, while *C1QTNF4* and *MADD* exhibited preferential expression in neurons (Fig. 1A and Fig. S1A). Co-expression analysis of these six causal genes, as well as *SPI1*, which were reported in our previous study [13], demonstrated strong correlations in neurons and these correlations were further enhanced in AD patient samples (Fig. 1B). We also performed co-expression analysis of these genes in other cell types (Fig. S1B). Although we observed similar co-expression pattern for genes in oligodendrocyte progenitor cells and immune cells, we did not find enhanced co-expression effect in AD patients. Note that most correlations of these genes did not reach significance in astrocytes and oligodendrocytes, due to the relatively small sample size and limited statistical power (Fig. S1B). Consistent with our prior observations at the single-cell, bulk mRNA, epigenetic, and protein levels [13], nearly all causal genes exhibited a consistent down-regulation in AD patient brains. This observation was further confirmed using newly available snRNA-seq datasets [42, 43], which demonstrated simultaneous down-regulation of these six causal genes in both neuronal and astrocytic populations of AD patients (Fig. 1C, D).

Given the potential role of these coordinated changes in AD pathogenesis, spatial transcriptomic analysis was conducted using Stereo-seq [20] in APP/PS1 mice to determine whether similar patterns were recapitulated in a murine AD model. Gene co-expression correlations were markedly increased in APP/PS1 mice compared to wild-type (WT) controls, mirroring the patterns observed in human AD brains (Fig. 1E, F). Subsequent evaluations at both the transcriptional and translational levels confirmed significant changes in gene expression in APP/PS1 mice. A significant reduction in *Mtch2*, *Ndufs3*, *Psmc3*, and *C1qtnf4* mRNA levels within the hippocampus and cortex (Fig. 1G and Fig. S1C) was revealed by qRT-PCR. Western blot analysis further confirmed the corresponding decrease in MTCH2, NDUFS3, and PSMC3 protein levels (Fig. 1H, I and Fig. S1D-E). In contrast, *Acp2* and *Madd* expression remained largely unchanged at both the mRNA and protein levels (Fig. 1G–I and Fig. S1C-E). Further validation using the MouseAC database (https://www.mouseac.org/) [44] revealed progressive down-regulation of *Mtch2*, *Ndufs3*, and *Psmc3* expression not only in APP/PS1 mice but also during normal aging (Fig. S1F). Notably, the mRNA levels of *Mtch2*, *Ndufs3*, *Psmc3*, and *C1qtnf4* exhibited significantly inverse correlations with both Aβ and Tau pathologies (Fig. S1G-H). Collectively, these findings suggest that the simultaneous down-regulation of *Mtch2*, *Ndufs3*, and *Psmc3* may contribute to AD pathogenesis through a synergistic mechanism.

To further confirm that these three genes share a synergistic molecular basis, we reanalyzed chromatin interactions among *MTCH2*, *NDUFS3*, and *PSMC3* using PLAC-seq data from microglia, neurons, and oligodendrocytes, and promoter capture Hi-C data from iPSC-derived hippocampal DG-like neurons, iPSC-induced cortical excitatory neurons, and human primary fetal astrocytes [45, 46]. The results showed that these three genes exhibit robust chromatin interactions across both neural and glial cell types (Fig. S2A), suggesting that their synergistic effects may be mediated by coordinated regulation of gene expression. We also utilized the online analysis tool STRING (https://string-db.org/) to construct a protein-protein interaction (PPI) network for MTCH2, NDUFS3, and PSMC3 in human and mouse (Fig. S2B). The three proteins formed an interconnected module in both species. To validate these interactions experimentally, we performed Co-IP assays in HEK293T cells overexpressing a combination of two of the three proteins (Fig. S2C-E). We confirmed the predicted interactions between all combinations of the three proteins (NDUFS3 and PSMC3, NDUFS3 and MTCH2, or PSMC3 and MTCH2). We speculated these physical interactions may represent the molecular basis for their synergistic effects.

Single gene knockdown disrupts mitochondrial function

To investigate the functional roles of *MTCH2*, *NDUFS3*, and *PSMC3* in AD pathogenesis and assess potential synergistic interactions, targeted knockdown experiments were performed in the human astrocyte-derived U251-APP cell line [19] (Fig. 2A). As *Acp2* expression remained unchanged in APP/PS1 mice and showed no correlation with Aβ and Tau pathology, *ACP2* knockdown was included as a negative control due to its high convergent functional genomics (CFG) score, ranking second only to *MTCH2* in our previous study [13]. To ensure robust gene silencing, three independent small siRNAs were screened for each target gene, and the most effective siRNA was selected based on knockdown efficiency (Fig. S3A). The final knockdown efficiencies were quantitatively validated for both single- and triple-gene perturbations (Fig. S3B). RNA-seq was subsequently performed to characterize transcriptomic alterations induced by these genetic perturbations (Fig. S3C). RNA-seq revealed that knockdown of *MTCH2*, *NDUFS3*, or *PSMC3* individually induced substantial transcriptomic alterations, with each perturbation generating a distinct set of DEGs. Notably, the most pronounced down-regulation consistently corresponded to the specifically targeted gene in each experimental condition (Fig. 2B–D).

Pathway enrichment analyses were performed on RNA-seq data from U251-APP cells with knockdown of each causal gene to investigate whether *MTCH2*, *NDUFS3*, and *PSMC3* contribute to AD pathogenesis through coordinated regulation of shared pathways. KEGG analysis indicated DEGs resulting from the knockdown of *MTCH2*, *NDUFS3*, or *PSMC3* were significantly enriched in neurodegeneration-associated pathways, including AD, Huntington's disease, Parkinson's disease, and multiple neurodegenerative disease pathways (Fig. 2E–G). Pathway-specific enrichment patterns aligned with the known molecular functions of these genes. *NDUFS3* knockdown led to significant enrichment of oxidative phosphorylation pathways, consistent with its role as a catalytic subunit of mitochondrial complex I [47]. Similarly, *PSMC3* knockdown showed specific enrichment in proteasome-related pathways, reflecting its function as a key component of the proteasome complex [48]. GO term analysis further demonstrated that knockdowns of *MTCH2*, *NDUFS3*, and *PSMC3* were associated with mitochondrial-related processes, including oxidative phosphorylation and electron transport chain activity, suggesting that each of these three genes is associated with mitochondrial function (Fig. 2H–J). These findings suggest that *MTCH2*, *NDUFS3*, and *PSMC3* may contribute to AD pathogenesis through the coordinated dysregulation of mitochondrial pathways.

To assess whether *ACP2* knockdown elicits transcriptomic alterations comparable to those observed for *MTCH2*, *NDUFS3*,

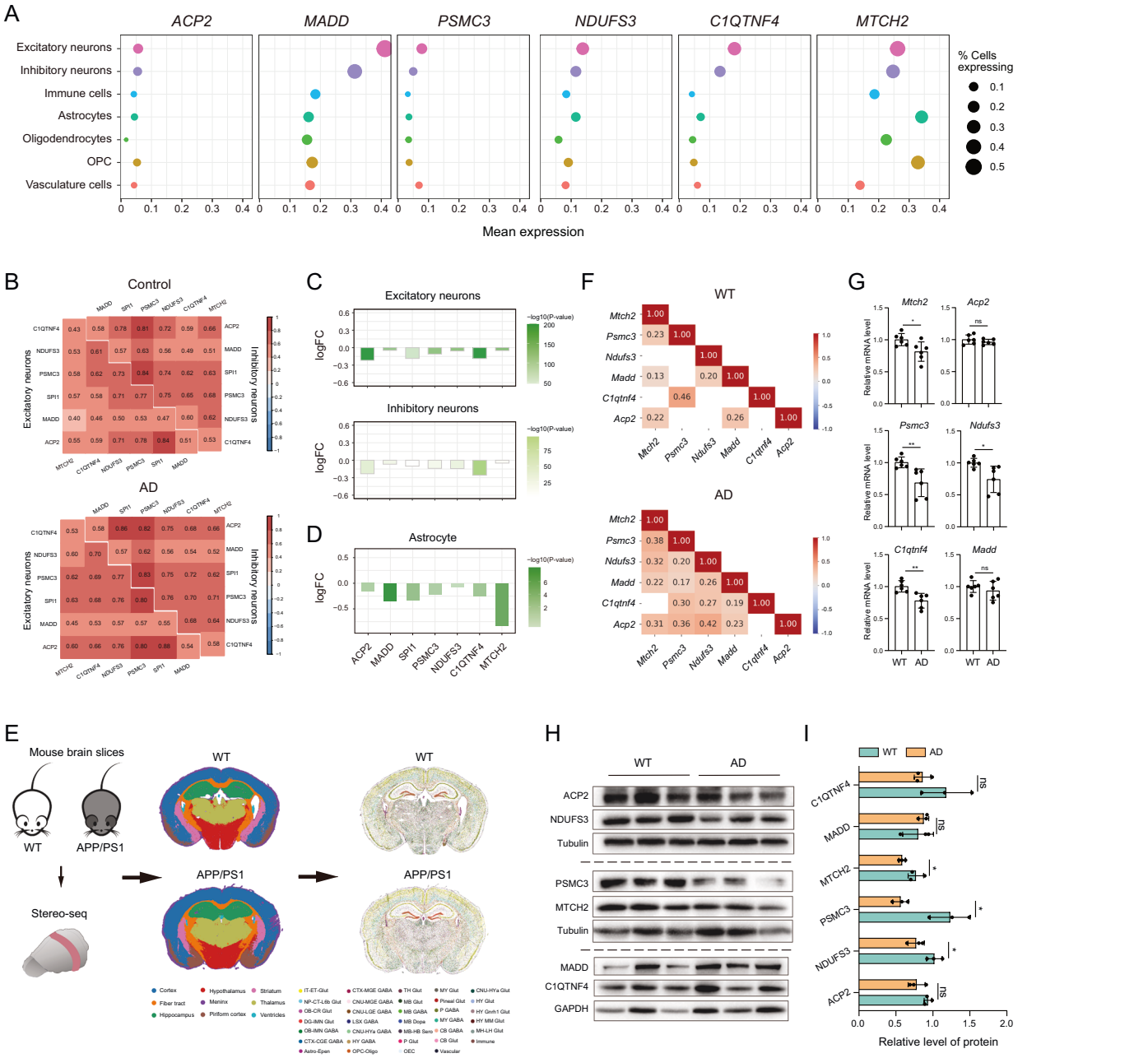

Fig. 1 Differential expression of six causal genes at 11p11.2 in AD patients and APP/PS1 mice. (A) Expression profiles of six causal genes at 11p11.2 across different brain cell types in healthy individuals, based on publicly available single-cell datasets [42]. **(B)** Correlation analysis of the expression of the six causal genes in excitatory and inhibitory neurons from healthy individuals and AD patients. **(C)** Down-regulation of the six causal genes at 11p11.2 in neuronal populations of AD patients. **(D)** Down-regulation of six causal genes at 11p11.2 in astrocytes of AD patients, derived from publicly available single-cell datasets [43]. **(E)** Spatial transcriptomic analysis of brain slices from APP/PS1 and wild-type (WT) mice. *Left*: Schematic representation of Stereo-seq spatial transcriptomic analysis; *Middle*: Unsupervised spatially constrained clustering of brain sections from APP/PS1 and WT mice, analyzed using Stereo-seq at bin 50 resolution; *Right*: Spatial visualization of segmented cell clusters identified through unsupervised clustering. Bins and cells are color-coded based on annotations from previous research [22]. Astro, astrocyte; CB, cerebellum; CGE, caudal ganglionic eminence; CNU, cerebral nuclei; CR, Cajal-Retzius; CT, corticothalamic; CTX, cerebral cortex; DG, dentate gyrus; Epen, ependymal; ET, extratelencephalic; HB, hindbrain; HY, hypothalamus; HYa, anterior hypothalamic; IMN, immature neurons; IT, intratelencephalic; L6b, layer 6b; LGE, lateral ganglionic eminence; LH, lateral habenula; LSX, lateral septal complex; MB, midbrain; MGE, medial ganglionic eminence; MH, medial habenula; MM, medial mammillary nucleus; MY, medulla; NP, near-projecting; OB, olfactory bulb; OEC, olfactory ensheathing cells; Oligo, oligodendrocytes; OPC, oligodendrocyte precursor cells; P, pons; TH, thalamus; Dopa, dopaminergic; GABA, GABAergic; Glut, glutamatergic; Sero, serotonergic. **(F)** Correlation analysis of the expression of the six causal genes at 11p11.2 in brain tissues from WT (*upper*) and APP/PS (AD) mice (*bottom*). **(G)** Relative mRNA expression levels of the six causal genes in the hippocampus of WT and APP/PS1 mice, measured by qRT-PCR (WT, $n = 6$; AD, $n = 6$). **(H-I)** Protein expression levels of the six causal genes at 11p11.2 in the hippocampus of WT and APP/PS1 mice (H) and corresponding quantitative analysis (I) (WT, $n = 3$; AD, $n = 3$). Each symbol denotes one mouse in (G) and (I); bar graphs represent mean ± standard deviation (SD). Statistical significance was determined using a two-tailed unpaired *t*-test (F, H); ns, not significant; *, $P < 0.05$; **, $P < 0.01$.

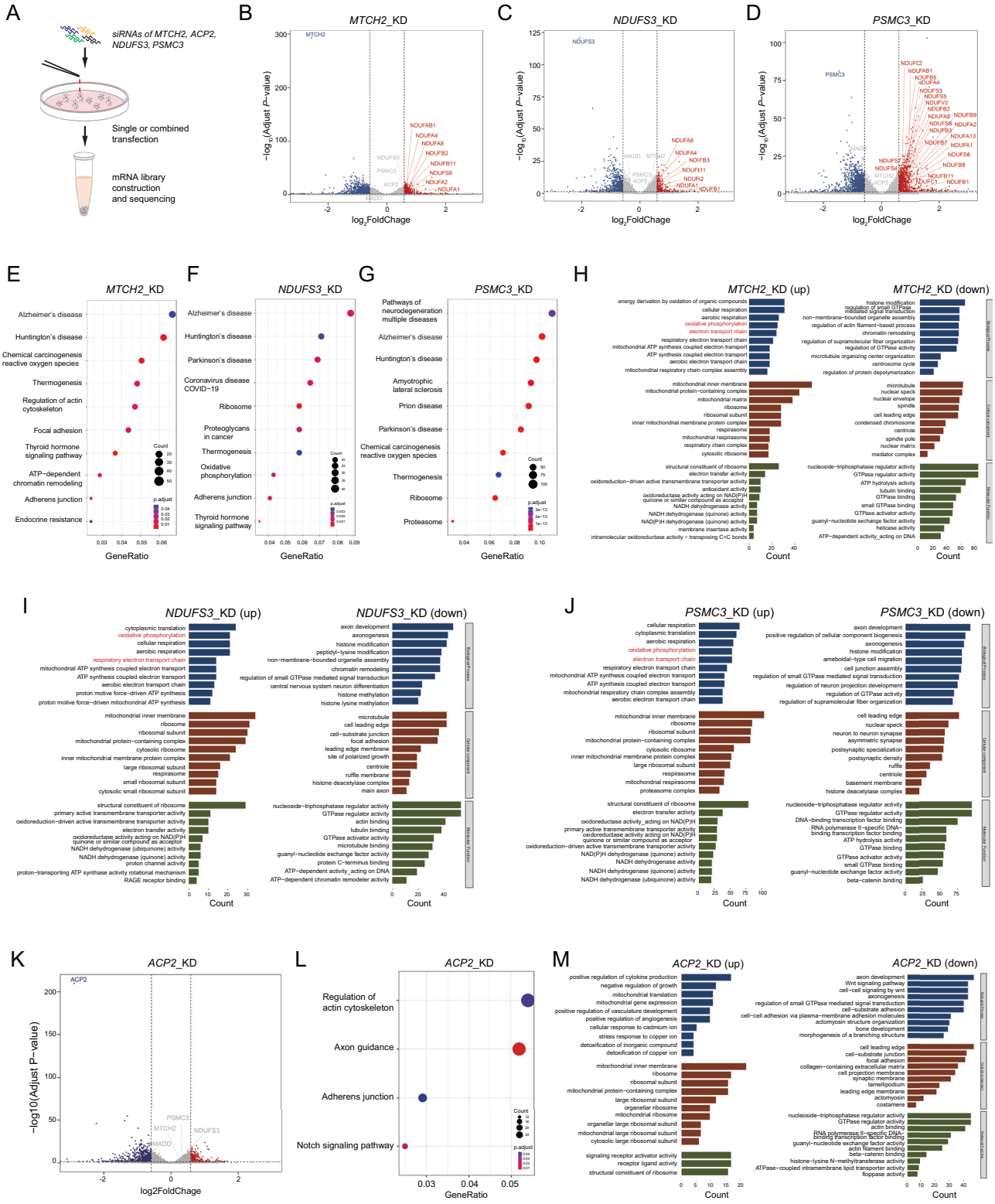

Fig. 2 Transcriptional alterations in U251-APP cells following individual or combined knockdown of *MTCH2*, *ACP2*, *NDUFS3*, and *PSMC3*. **(A)** Schematic representation of individual and combined knockdown of causal genes at 11p11.2 in U251-APP cells. **(B-D)** Volcano plots depicting DEGs following individual knockdown (KD) of *MTCH2* (B), *NDUFS3* (C), and *PSMC3* (D). NDUF-related genes are highlighted in red. **(E-G)** KEGG enrichment analysis of differentially expressed genes (DEGs) in U251-APP cells following knockdown of *MTCH2* (E), *NDUFS3* (F), and *PSMC3* (G). **(H-J)** GO enrichment analysis of up-regulated (up) and down-regulated (down) DEGs following knockdown of *MTCH2* (H), *NDUFS3* (I), and *PSMC3* (J). **(K)** Volcano plot depicting DEGs in U251-APP cells following *ACP2* knockdown. **(L)** KEGG enrichment analysis of DEGs following *ACP2* knockdown. **(M)** GO enrichment analysis of up-regulated (up) and down-regulated (down) DEGs following *ACP2* knockdown.

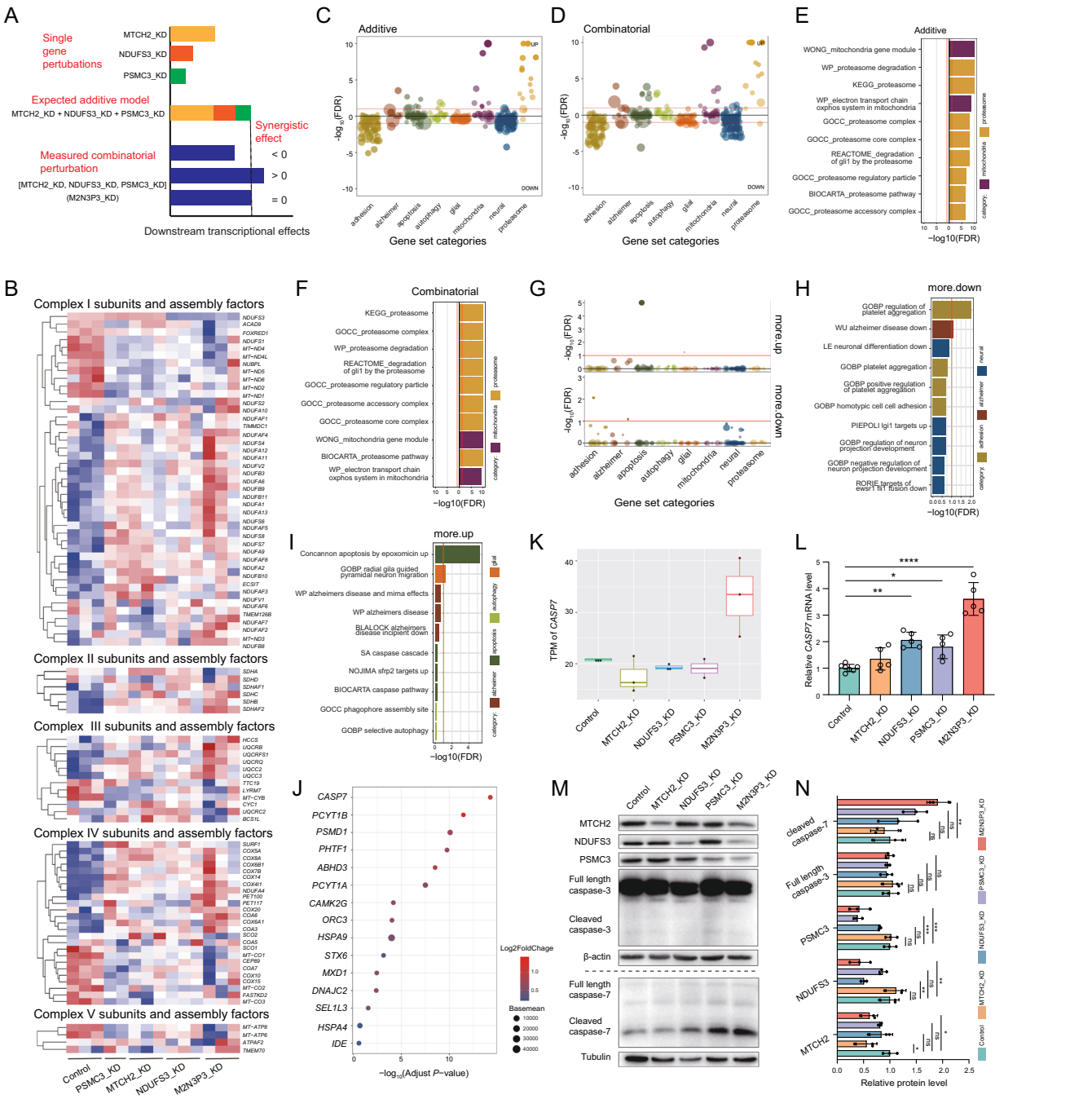

and *PSMC3*, RNA-seq data from *ACP2* knockdown U251-APP cells were analyzed using the same analytical pipeline (Fig. 2K–M). Unlike *MTCH2*, *NDUFS3*, and *PSMC3*, differential gene expression following *ACP2* perturbation did not show significant enrichment in AD-related pathways, neurodegeneration-associated networks, or the oxidative phosphorylation and electron transport chain pathways (Fig. 2L, M). Both KEGG and GO enrichment analyses revealed distinct transcriptomic patterns following *ACP2* knockdown, diverging significantly from the patterns observed for the other causal genes (Fig. 2L, M). Comparative analyses further reinforced the stronger association of *MTCH2*, *NDUFS3*, and *PSMC3* with AD pathogenesis. The enrichment of mitochondrial functional pathways exclusively in cells subjected to *MTCH2*, *NDUFS3*, and *PSMC3* knockdown suggested their involvement in shared mitochondrial regulatory mechanisms, potentially contributing to disease-related mitochondrial dysfunction. Based on these findings, subsequent investigations focused on the synergistic effects of *MTCH2*, *NDUFS3*, and *PSMC3* to elucidate their collective role in AD pathogenesis.

Synergistic regulation of caspase-7-mediated apoptotic pathways by *MTCH2*, *NDUFS3*, and *PSMC3*

To investigate the synergistic effects of *MTCH2*, *NDUFS3*, and *PSMC3*, a recently developed synergistic analysis model [14] was employed (Fig. S3D). This analytical framework facilitates the identification of downstream transcriptional convergence and synergistic effects following gene perturbations and has been successfully applied in studies of schizophrenia-associated risk genes [14–16]. The expected transcriptomic effects under an additive model, derived from individual gene knockdowns, were

Fig. 3 Synergistic regulation of mitochondrial function and apoptosis by *MTCH2*, *NDUFS3*, and *PSMC3*. **(A)** Schematic representation of synergistic effect analysis based on DEGs in U251-APP cells. Conditions include individual knockdown of *MTCH2* (MTCH2_KD), *NDUFS3* (NDUFS3_KD), and *PSMC3* (PSMC3_KD), and combined knockdown of all three genes ([MTCH2_KD, NDUFS3_KD, PSMC3_KD] (M2N3P3_KD)). Comparison between expected additive model and measured combinational perturbation enables detection of synergistic effects on gene expression [14]. **(B)** mRNA expression levels of mitochondrial complex I–V subunits and assembly factors following individual knockdown of *MTCH2* (MTCH2_KD), *NDUFS3* (NDUFS3_KD), and *PSMC3* (PSMC3_KD), or combined knockdown of all three genes (M2N3P3_KD). Control: U251-APP cells transfected with control siRNA. **(C-D)** Competitive GSEA of DEGs from additive (C) and combinatorial (D) comparisons. **(E)** Bar charts depicting 10 most significantly enriched gene sets in (C), ranked by FDR values. Red lines denote an enrichment FDR threshold of 0.1. **(F)** Bar charts depicting 10 most significantly enriched gene sets in (D). Annotations are the same as (E). **(G)** Competitive GSEA of DEGs categorized as "more up-regulated" (more up) and "more down-regulated" (more down), as defined in Supplementary Figure 3B. **(H-I)** Over-representation analysis of DEGs categorized as "more down-regulated" (more down) (H) and "more up-regulated" (more up) (I) in (G). Top 10 enriched pathways are ranked by FDR values, with red lines denoting an enrichment FDR threshold of 0.1. **(J)** Expression changes in genes associated with apoptosis pathway, identified in (I), ranked by *P*-values adjusted by Benjamini-Hochberg correction. **(K-L)** mRNA expression levels of *CASP7* in U251-APP cells following individual or combined knockdown of *MTCH2*, *NDUFS3*, and *PSMC3*, based on RNA-seq data (K; Control: $n = 3$; MTCH2_KD: $n = 3$; NDUFS3_KD: $n = 3$; PSMC3_KD: $n = 2$; M2N3P3_KD: $n = 3$) of Fig. 2A and qRT-PCR validation (L; Control: $n = 7$; MTCH2_KD: $n = 5$; NDUFS3_KD: $n = 5$; PSMC3_KD: $n = 5$; M2N3P3_KD: $n = 5$). TPM, transcripts per million. **(M-N)** Protein expression levels of caspase-7, caspase-3, MTCH2, NDUFS3, and PSMC3 in U251-APP cells following individual or combined knockdown of *MTCH2*, *NDUFS3*, and *PSMC3* (M) and corresponding quantitative analysis (N) ($n = 3$ per group). Values are presented as mean ± SD. Statistical significance was determined using one-way ANOVA (L, N); ns, not significant; *, $P < 0.05$; **, $P < 0.01$; ***, $P < 0.001$; ****, $P < 0.0001$.

compared to the observed transcriptional changes following triple knockdown of *MTCH2*, *NDUFS3*, and *PSMC3* (Fig. 3A). This approach enabled the identification of gene expression alterations that exceeded the predicted additive effects, providing evidence for functional synergy among these genes. Knockdown efficiency was confirmed to be consistent across single and triple knockdown conditions (Fig. S3B). Given that the individual knockdown of *MTCH2*, *NDUFS3*, and *PSMC3* significantly enriched genes involved in oxidative phosphorylation (OXPHOS) and electron transport chain (which links nutrient oxidation to ATP production by OXPHOS and consists of complexes I-V in the mitochondrial inner membrane) pathways (Fig. 2H–J), the expression patterns of mitochondrial complexes subunits and assembly factors [49] were examined in detail. We observed a synergistic up-regulation trend in mRNA expression in several *NDUF* (NADH: ubiquinone oxidoreductase subunit) genes encoding mitochondrial complex I components following individual and triple gene knockdowns (Fig. 3B), suggesting that these three genes individually or collectively modulate mitochondrial complex I function through an uncharacterized mechanism. We speculated that synergistic up-regulation of the related *NDUF* genes upon individual or triple knockdown of *MTCH2*, *NDUFS3*, and *PSMC3* would offer a compensatory effect for the impaired mitochondrial respiratory function.

Transcriptomic analysis using the synergistic analysis model revealed that about 11% of genes exhibited expression changes greater than those predicted under the additive model, with 678 genes showing enhanced up-regulation (more up, $n = 678$) and 703 genes exhibiting greater down-regulation (more down, $n = 703$; synergy false discovery rate (FDR) < 0.1) (Fig. S4A-G). Competitive GSEA using datasets from the GSEA-MSigDB database (https://www.gsea-msigdb.org/gsea/msigdb/collections.jsp), demonstrated that DEGs from both the additive model and the triple-knockdown condition were significantly enriched in mitochondrial and proteasome-related pathways, consistent with the established subcellular localization of *MTCH2*, *NDUFS3*, and *PSMC3* (Fig. 3C–F). Among synergistically dysregulated pathways, apoptosis by epoxomicin (proteasome inhibitor) up [50] emerged as the most significantly enriched process, alongside pathways related to cell adhesion, AD, and glial cell function (Fig. 3G–I). The enrichment of this proteasome inhibition-induced apoptosis aligned with previous studies showing association of proteasome dysfunction with AD [51–53]. Given the well-established role of proteasome dysfunction in AD pathogenesis, epoxomicin-induced apoptosis—as a well-established model of proteasome impairment—is directly relevant to the neurodegenerative processes underlying AD. Further examination of apoptosis-related DEGs revealed that *CASP7* was the most prominently up-regulated gene following triple knockdown (Fig. 3J, K). These findings were experimentally validated in U251-APP cells using qRT-PCR and Western blotting (Fig. 3L–N, Fig. S4H-I). As apoptosis is primarily executed by caspase-3 or/and caspase-7, both of which cleave essential cellular substrates to initiate programmed cell death [54, 55], the specificity of caspase-7 activation was further investigated. Western blot analysis showed that the caspase-3 protein levels unaltered, whereas caspase-7 activation was the most pronounced following triple gene knockdown, followed by individual knockdown of *PSMC3* (Fig. 3M, N and Fig. S4H-I). Notably, the cleaved caspase-9 was also remarkably increased following triple gene knockdown (Fig. S4H-I). Together, these findings indicate that the simultaneous reduction of *MTCH2*, *NDUFS3*, and *PSMC3* disrupts mitochondrial complex I function, potentially triggering apoptosis through activation of caspase-7, thereby contributing to AD pathogenesis.

Validation of the synergistic regulation of *MTCH2*, *NDUFS3*, and *PSMC3* in mitochondrial function and apoptosis

Mitochondrial complex I, the largest component of the respiratory chain, serves as the primary site for ROS generation [56]. To investigate the regulatory roles of *MTCH2*, *NDUFS3*, and *PSMC3* in mROS production, mROS levels were assessed using the fluorescent probe MitoSOX, with fluorescence signals quantified by confocal microscopy and flow cytometry (Fig. 4A, B). Cells treated with oligomycin and antimycin A (OA), known inducers of mROS [26, 57, 58], exhibited a substantial increase in fluorescence intensity, confirming assay sensitivity (Fig. 4A–D). MitoSOX fluorescence intensity was markedly elevated following individual gene knockdown, with further intensification observed in the triple knockdown cells (Fig. 4C). However, flow cytometry analysis of MitoSOX$^+$ cells demonstrated increased mROS levels in all individual gene knockdown groups but failed to show further enhancement in the triple knockdown group (Fig. 4D). This discrepancy may reflect limitations in transfection efficiency, warranting further optimization in future studies. To further demonstrate a cooperative role of MTCH2, NDUFS3, and PSMC3 in regulating mROS, we overexpressed the three genes in U251-APP cells and treated with or without OA. We found that triple gene overexpression led to a significant reduction in mROS compared to individual gene overexpression (Fig. S5A-C). These results demonstrated that overexpression of these genes ameliorates the oxidative stress phenotype, supporting their cooperative role in mitochondrial protection.

To validate the impact of individual and triple gene knockdowns on apoptotic pathways identified through the synergistic analysis model, apoptosis levels were evaluated using Annexin V-FITC/PI double staining and flow cytometry. Triple gene

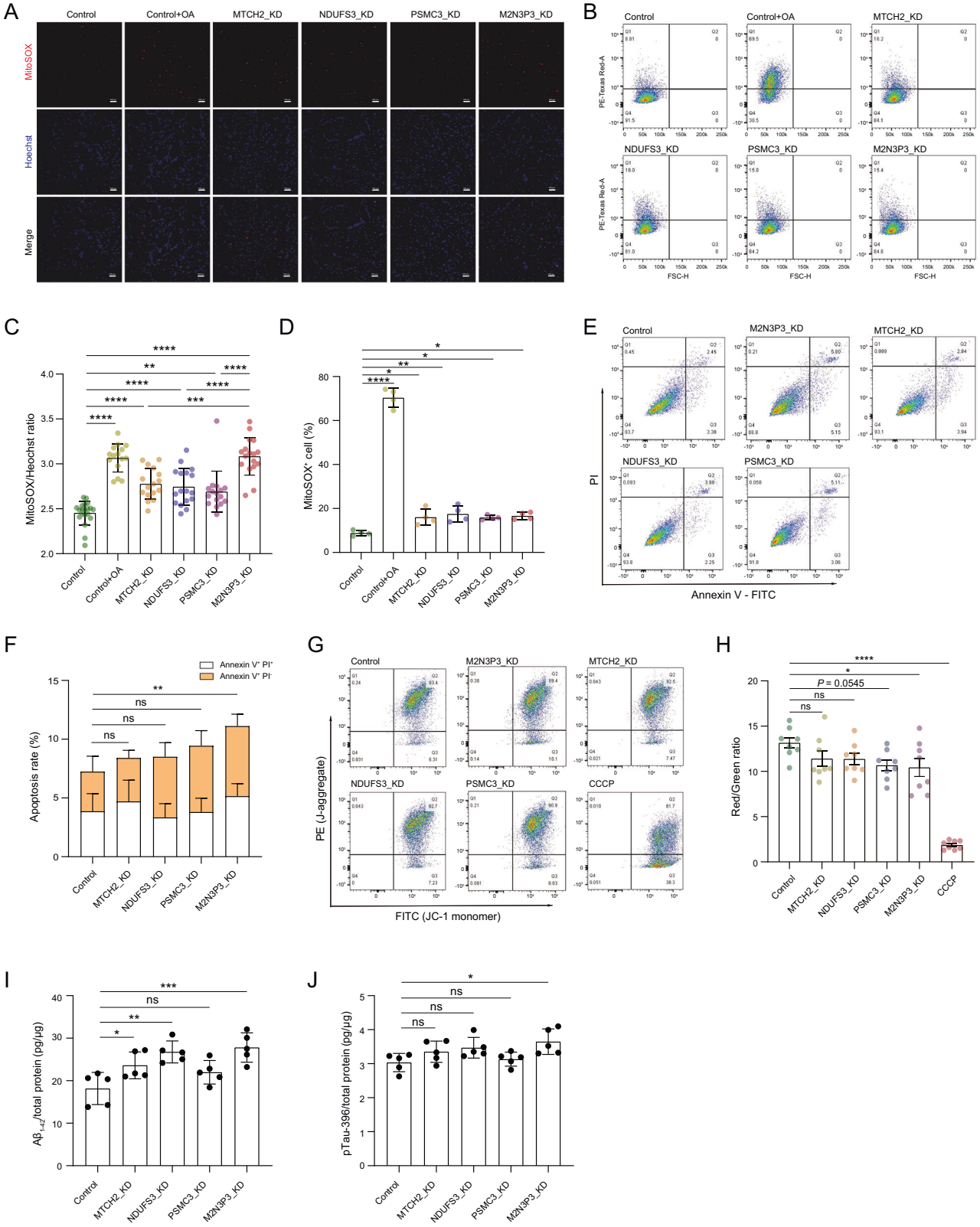

knockdown significantly promoted apoptosis in U251-APP cells (Fig. 4E–F). To determine whether apoptosis was driven by excessive mROS production, OA (mROS inducer) [57, 58], melatonin (mitochondrial antioxidant) [59–61], and Q-VD-OPh (caspase inhibitor with potent caspase-7 inhibition) [39, 40] were used as experimental controls. Consistent with expectations, Q-VD-OPh significantly suppressed apoptosis, while melatonin showed a modest protective effect under basal conditions but markedly reduced apoptosis in OA-treated cells (Fig. S5D-E). These findings support the hypothesis that excessive mROS contributes

Fig. 4 Synergistic regulation of mROS levels and apoptosis by *MTCH2*, *NDUFS3*, and *PSMC3*. **(A-B)** Representative confocal microscopy images (A) and flow cytometry plots (B) of MitoSOX staining in U251-APP cells following individual knockdown of *MTCH2* (MTCH2_KD), *NDUFS3* (NDUFS3_KD), and *PSMC3* (PSMC3_KD), as well as combined knockdown of all three genes (M2N3P3_KD). Control: U251-APP cells transfected with control siRNA. **(C)** Quantification of MitoSOX fluorescence intensity from (A). Each group was analyzed across 15–20 fields from three independent slides (control, $n = 20$ fields; control + OA, $n = 15$ fields; MTCH2_KD, $n = 16$ fields; NDUFS3_KD, $n = 17$ fields; PSMC3_KD, $n = 16$ fields; M2N3P3_KD, $n = 17$ fields). OA, Oligomycin + Antimycin A. **(D)** Quantification of MitoSOX$^+$ cells from (B) via flow cytometry analysis. Each group contains four biological replicates. **(E)** Flow cytometry of U251-APP cells following individual knockdown of *MTCH2* (MTCH2_KD), *NDUFS3* (NDUFS3_KD), and *PSMC3* (PSMC3_KD), as well as combined knockdown of all three genes (M2N3P3_KD). Cells were double-stained with Annexin V and propidium iodide (PI). Cells underwent early and late stages of apoptosis were defined as Annexin V$^+$ PI$^-$ and Annexin V$^+$ PI$^+$, respectively. **(F)** Quantification of apoptosis rate in (E) ($n = 8$ per group). **(G-H)** Representative flow cytometry plots (G) and quantification (H) of JC-1 staining in U251-APP cells following individual knockdown of *MTCH2* (MTCH2_KD), *NDUFS3* (NDUFS3_KD), and *PSMC3* (PSMC3_KD), and triple gene knockdown (M2N3P3_KD) ($n = 8$ per group). Control, U251-APP cells transfected with control siRNA. CCCP was used as a positive control. **(I-J)** Levels of $A\beta_{1\text{-}42}$ in culture supernatant (I) and pTau-396 in cell lysate (J) of U251-APP cells following individual knockdown of *MTCH2* (MTCH2_KD), *NDUFS3* (NDUFS3_KD), and *PSMC3* (PSMC3_KD), as well as combined knockdown of all three genes (M2N3P3_KD). $A\beta_{1\text{-}42}$ and pTau-396 levels were measured by ELISA ($n = 5$ per group). Data in (C-D, F and H-J) are presented as mean ± SD, quantified by one-way ANOVA; ns, not significant; *, $P < 0.05$; **, $P < 0.01$; ***, $P < 0.001$; ****, $P < 0.0001$.

to apoptosis in U251-APP cells [62]. We validated these findings using human neuroblastoma cell line SH-SY5Y with individual and triple gene knockdowns, and assessed the levels of cleaved caspase-7 and apoptosis. Consistent with U251-APP cells, triple gene knockdown of *MTCH2*, *NDUFS3*, and *PSMC3* in SH-SY5Y cells led to significantly elevated levels of cleaved caspase-7 protein and apoptosis (Fig. S6A-D).

We further investigated the upstream apoptotic events linking mitochondrial dysfunction to caspase-7 activation, and examined MMP loss and mitophagy in U251-APP cells following single and combined knockdown of *MTCH2*, *NDUFS3*, and *PSMC3*. We observed that triple gene knockdown induced a more pronounced decrease in MMP compared to any single-gene knockdown (Fig. 4G, H). However, we found no significant differences in the mitochondrial levels of the key mitophagy regulators (PINK1 and Parkin) between individual and triple gene knockdown (Fig. S6E-F). These findings indicated that mitochondrial impairment may serve as an upstream event in our models.

Our previous study demonstrated that knockdown of *MADD*, *PSMC3*, or *MTCH2* alone significantly increased $A\beta_{1\text{-}42}$ levels in U251-APP cells, whereas knockdown of *MTCH2* or *PSMC3* alone did not alter phosphorylated tau (pTau-396) levels [13]. Here, triple knockdown of *MTCH2*, *NDUFS3*, and *PSMC3* not only significantly increased $A\beta_{1\text{-}42}$ levels but also led to a significant elevation in pTau-396 levels (Fig. 4I, J and Fig. S7A-B). These observations suggest that the simultaneous down-regulation of these genes exerts a stronger impact on AD pathogenesis than individual gene perturbations, reinforcing the concept that polygenic synergistic effects play a critical role in disease progression.

Q-VD-OPh administration ameliorates cognitive deficits in APP/PS1 mice

Given the observed synergistic regulation of caspase-7-mediated apoptosis by *MTCH2*, *NDUFS3*, and *PSMC3*, we hypothesized that suppressing caspase-7 activity may ameliorate AD pathology. Several lines of evidence support this hypothesis. First, a rare missense variant in *CASP7* has been reported to be associated with familial late-onset AD [63]. Second, *CASP7* expression was significantly increased in various brain regions in AD patients [29] and was also significantly elevated in AD mice (homozygous TASTPM mice) older than 8 months of age [44] (Fig. 5A, B). In contrast, *CASP3* expression in different brain regions of AD patients remained comparable to that of healthy individuals, and this gene showed no expressional change after the massive emergence of AD pathology (8 months) in AD mice, despite being elevated in younger AD mice (Fig. S8A-B). The pathologies of Aβ and Tau were positively correlated with the expression level of *Casp7*, but not with the expression of *Casp3* in AD mice (Fig. 5C and Fig. S8C-D). Third, the expression of *CASP7* showed an increasing trend during aging in humans, while *CASP3* showed a decreasing trend (Fig. 5D and Fig. S8E). Collectively, these findings suggest that caspase-7-mediated apoptosis may contribute to AD pathogenesis.

To test whether pharmacological inhibition of caspase-mediated apoptosis could ameliorate cognitive impairment, Q-VD-OPh was administered to APP/PS1 mice (Fig. 5E). Notably, Q-VD-OPh had no effect on body weight (Fig. 5F). Cognitive function was assessed in 6-month-old APP/PS1 mice after 1 month of Q-VD-OPh treatment using the NOR test (Fig. 5E). APP/PS1 mice exhibited a significantly lower recognition index compared to WT controls, indicating impaired recognition memory. However, this deficit was partially rescued by Q-VD-OPh treatment (Fig. 5G, H). Importantly, there were no significant differences in movement velocity or total distance traveled between treated and untreated APP/PS1 mice, confirming that the improvement in recognition index was not due to changes in general locomotor activity (Fig. 5G, H).

To further evaluate spatial learning and memory, the MWM test was performed [17, 24]. During the training phase, swimming velocity did not differ significantly among APP/PS1 mice, Q-VD-OPh-treated APP/PS1 mice, and WT controls (Fig. 5I), indicating no differences in general activity. However, untreated APP/PS1 mice exhibited a longer escape latency compared to WT mice, which was reduced following Q-VD-OPh treatment (Fig. 5J). In both the 4-h and 72-h probe trials, untreated APP/PS1 mice showed fewer platform crossings and spent less time in the target quadrant, whereas Q-VD-OPh-treated APP/PS1 mice exhibited more frequent crossings and prolonged target quadrant exploration, demonstrating improved memory retention (Fig. 5K, L).

To assess the long-term effects of Q-VD-OPh, behavioral testing was repeated following 3 months of treatment. Results mirrored those obtained after the 1-month treatment period. In the NOR test, WT and Q-VD-OPh-treated APP/PS1 mice spent significantly more time exploring the novel object, whereas untreated APP/PS1 mice exhibited no preference (Fig. S9A-B). Swimming speed remained comparable across all groups (Fig. S9C), but a significantly impaired learning ability was observed in APP/PS1 mice compared to WT mice, and this trend was alleviated by the Q-VD-OPh treatment (Fig. S9D). Similarly, during the 4-h and 72-h probe trials, untreated APP/PS1 mice displayed shorter target quadrant exploration times and fewer platform crossings, while Q-VD-OPh-treated APP/PS1 mice performed significantly better, indicating enhanced spatial memory (Fig. S9E-F). Collectively, these findings indicate that Q-VD-OPh enhances both recognition and spatial memory in APP/PS1 mice. However, given that memory impairment typically worsens with disease progression, its long-term efficacy remains uncertain. As APP/PS1 mice were treated early and behavioral assessments were conducted at

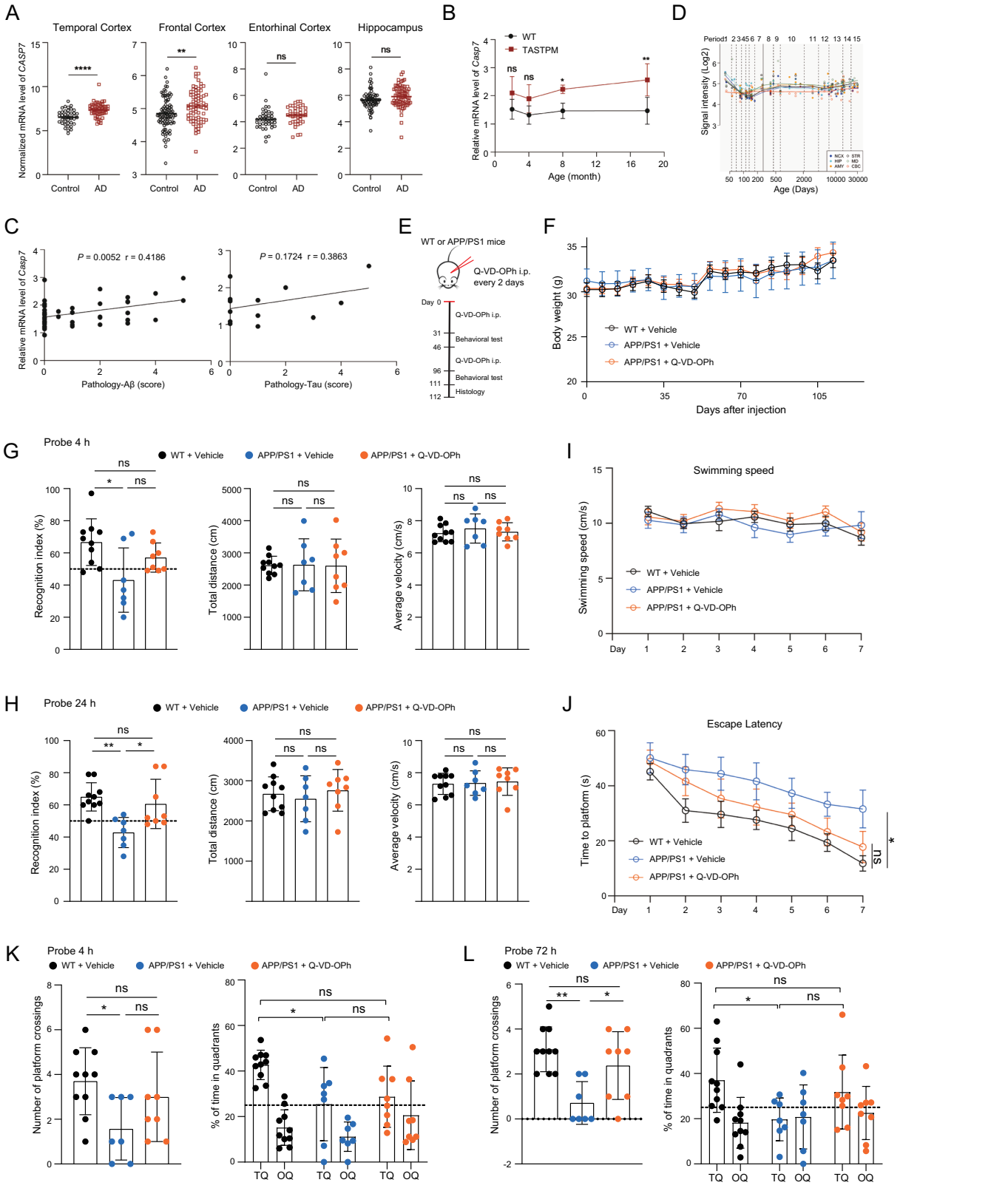

6 months of age, multiple factors may have influenced cognitive and spatial memory outcomes. Further studies using refined methodologies are needed to clarify the sustained impact of prolonged Q-VD-OPh administration on memory function in APP/PS1 mice.

Q-VD-OPh reduces apoptosis and Aβ plaque deposition in APP/PS1 mice

To assess the systemic effects of Q-VD-OPh treatment, major organ weights were analyzed, revealing no significant differences in organ indices (organ weight/body weight) among WT, APP/PS1,

Fig. 5 Apoptosis inhibitor Q-VD-OPh mitigates cognitive and memory impairments in APP/PS1 mice. (A) mRNA expression levels of *CASP7* in the entorhinal cortex, frontal cortex, temporal cortex, and hippocampus of AD patients (AD) and healthy controls (Control), based on compiled datasets [29]. Values are presented as mean ± SD; statistical significance was determined using a two-tailed unpaired *t*-test; ns, not significant; **, $P < 0.01$; ****, $P < 0.0001$. **(B)** mRNA expression levels of *Casp7* in brain tissues of WT and homozygous TASTPM mice (homozygous $APP^{k670N/M671L}$ and $PSEN1^{M146V}$ mutations) at different ages (2 months, WT, $n = 8$, TASTPM, $n = 4$; 4 months, WT, $n = 7$, TASTPM, $n = 4$; 8 months, WT, $n = 8$, TASTPM, $n = 4$; 18 months, WT, $n = 7$, TASTPM, $n = 2$), retrieved from the MouseAC dataset [44]. Values are presented as mean ± SD, quantified by two-way ANOVA with Sidak's multiple comparisons test; ns, not significant; *, $P < 0.05$; **, $P < 0.01$. **(C)** Correlation analysis of *Casp7* mRNA levels with Aβ pathology (*left*) and Tau pathology (*right*) in AD mice. Data for *Casp7* mRNA levels and Aβ pathology were obtained from APP mutant mice (13 homozygous $APP^{k670N/M671L}$, 14 homozygous $APP^{k670N/M671L}$-$PSEN1^{M146V}$, and 16 heterozygous $APP^{k670N/M671L}$-$PSEN1^{M146V}$ mutant mice), while data for *Casp7* mRNA levels and Tau pathology were obtained from 14 $MAPT^{P301L}$ mutant mice, retrieved from the MouseAC dataset [44] for Pearson's correlation test. **(D)** Developmental and age-related expression patterns of *CASP7* mRNA in the human brain, based on the HBT dataset [98]. **(E)** Experimental timeline for WT and APP/PS1 mice treated with or without Q-VD-OPh. **(F)** Body weight measurements of WT and APP/PS1 mice with or without Q-VD-OPh administration (WT + Vehicle, $n = 10$; APP/PS1 + Vehicle, $n = 7$; APP/PS1 + Q-VD-OPh, $n = 8$). Data are presented as mean ± standard error of the mean (SEM), quantified by one-way ANOVA. **(G-H)** Recognition index, total distance traveled, and average velocity during novel object recognition test at the 4-h (G) and 24-h (H) probe trials in the same cohort as (F). **(I-J)** Swimming speed (I) and escape latency (J) of APP/PS1 and WT mice during the training phase of the Morris water maze test. Data are presented as mean ± SEM, quantified by one-way ANOVA; ns, not significant; *, $P < 0.05$. **(K-L)** Number of target crossings and time spent in the target quadrant of the Morris water maze during 4-h (K) and 72-h (L) probe trials. TQ, target quadrant; OQ, opposite quadrant. Data in (G-H and K-L) are presented as mean ± SD, quantified by one-way ANOVA, ns, not significant; *, $P < 0.05$; **, $P < 0.01$.

and Q-VD-OPh-treated APP/PS1 mice (Fig. S10A). Routine blood analysis showed no marked differences in white or red blood cell counts among groups; however, platelet counts were significantly reduced in APP/PS1 mice compared to WT controls (Fig. S10B). This observation is consistent with previous findings linking platelet abnormalities to AD pathology [64], suggesting that platelet indices may serve as potential AD biomarkers. Additionally, serum levels of key biochemical markers, including aspartate aminotransferase, alanine aminotransferase, total protein, albumin, and globulin, remained unchanged across groups (Fig. S10C). Histological analysis of liver and kidney tissues confirmed the absence of Q-VD-OPh-induced pathological alterations in APP/PS1 mice (Fig. S10D-E), supporting its systemic safety profile.

To investigate whether Q-VD-OPh modulates apoptosis in the AD brain, caspase-7 and caspase-3 protein levels were examined in the hippocampus and cortex of APP/PS1 mice. Western blot analysis revealed that cleaved caspase-7 levels were significantly elevated in hippocampus of APP/PS1 mice relative to WT controls, and this increase was effectively attenuated by Q-VD-OPh administration (Fig. 6A, B). Similarly, cleaved caspase-3 levels were also significantly reduced following Q-VD-OPh treatment (Fig. 6A–D), indicating a robust anti-apoptotic effect. Given that Aβ plaque accumulation is a key pathological hallmark of AD, immunofluorescence analysis was performed to determine the potential influence of Q-VD-OPh treatment on Aβ deposition in APP/PS1 mice. While western blot analysis revealed a non-significant trend toward lower APP protein levels in the hippocampus and cortex following treatment (Fig. 6A–D), $4G8^{+}$ immunofluorescence staining showed a significant reduction in Aβ plaque burden in both regions after Q-VD-OPh administration (Fig. 6E and G–H). These findings suggest that Q-VD-OPh mitigates Aβ pathology in the APP/PS1 mouse model. Neuronal apoptosis plays a critical role in AD progression [65–67]. To assess whether Q-VD-OPh treatment preserved neuronal populations, NeuN-positive cells were quantified in the hippocampal CA3 region. Results indicated that the number of NeuN-positive cells was significantly lower in APP/PS1 mice compared to WT controls and Q-VD-OPh-treated APP/PS1 mice (Fig. 6F and I), suggesting that Q-VD-OPh attenuates hippocampal neuronal loss in AD mice.

To further delineate the molecular effects of Q-VD-OPh, RNA-seq analysis was conducted on cortical and hippocampal tissues. DEG analysis revealed distinct transcriptomic alterations following Q-VD-OPh treatment (Fig. S11A-B). KEGG and GO enrichment analyses identified significant enrichment in neurodegenerative-related pathways, including AD, Parkinson's disease, and Huntington's disease, as well as pathways involved in MAPK signaling and synapse organization (Fig. 6J–M; Table S3). DEGs associated with AD and apoptosis pathways were further characterized in APP/PS1 mice with and without Q-VD-OPh treatment (Fig. 6N–O). Notably, mRNA levels of *Ctsh* and *Ctsl* were markedly up-regulated in the hippocampus of APP/PS1 mice, in line with our recent study [68]. However, Q-VD-OPh treatment significantly reduced *Ctsh* and *Ctsl* mRNA expression. As members of the cathepsin superfamily, CTSH and CTSL are lysosomal proteins involved in protein degradation via proteolysis, suggesting that Q-VD-OPh-mediated inhibition of apoptosis may involve lysosomal pathways. We further investigated the potential feedback effects of Q-VD-OPh treatment on the protein levels of MTCH2, NDUFS3, and PSMC3 in APP/PS1 mice. The results showed that treatment of Q-VD-OPh had no apparent effect on protein levels of MTCH2, NDUFS3, and PSMC3 in the cortex and hippocampus tissues of APP/PS1 mice with or without Q-VD-OPh (Fig. S11C-F). This result indicated that the observed benefits of Q-VD-OPh are unlikely to be mediated by altered expression of these proteins. Taken together, these findings highlight a potential mechanism by which Q-VD-OPh modulates lysosomal function to improve AD-related phenotypes.

DISCUSSION

GWAS and multi-omics analyses have identified thousands of genes associated with AD, yet the precise functional roles of most risk genes remain unclear [4, 5, 69]. While *APP*, *PSEN1*, and *PSEN2* are well-established causal genes in early-onset familial AD [2, 10–12, 70–72], pathogenic mutations in these genes account for less than 5% of total AD cases. In contrast, late-onset sporadic AD, which comprises over 95% of cases, is driven by a polygenic architecture, involving a large number of risk genes exerting weaker individual effects [4, 5, 73–75]. Given that the influence of a single low-risk gene on AD pathogenesis is minimal and that each risk locus harbors multiple functionally relevant genes, it is plausible that synergistic interactions among genes within the same locus play a more substantial role in disease progression. Our previous study identified multiple functional variants at the 11p11.2 locus that regulate the expression of several causal genes, including *MTCH2*, *ACP2*, *NDUFS3*, *PSMC3*, *C1QTNF4*, and *MADD* [13]. The present findings provide experimental evidence supporting the synergistic role of multiple causal genes (*MTCH2*, *NDUFS3*, and *PSMC3*) at this locus in regulating mROS production and apoptosis, key mechanisms implicated in AD pathogenesis (Fig. 7). These results support the hypothesis that multiple genetic variants and causal genes within a single locus collectively contribute to AD risk rather than acting independently. To our knowledge, this is the first systematic experimental validation of polygenic synergism within a single risk locus in AD genetics research. While prior

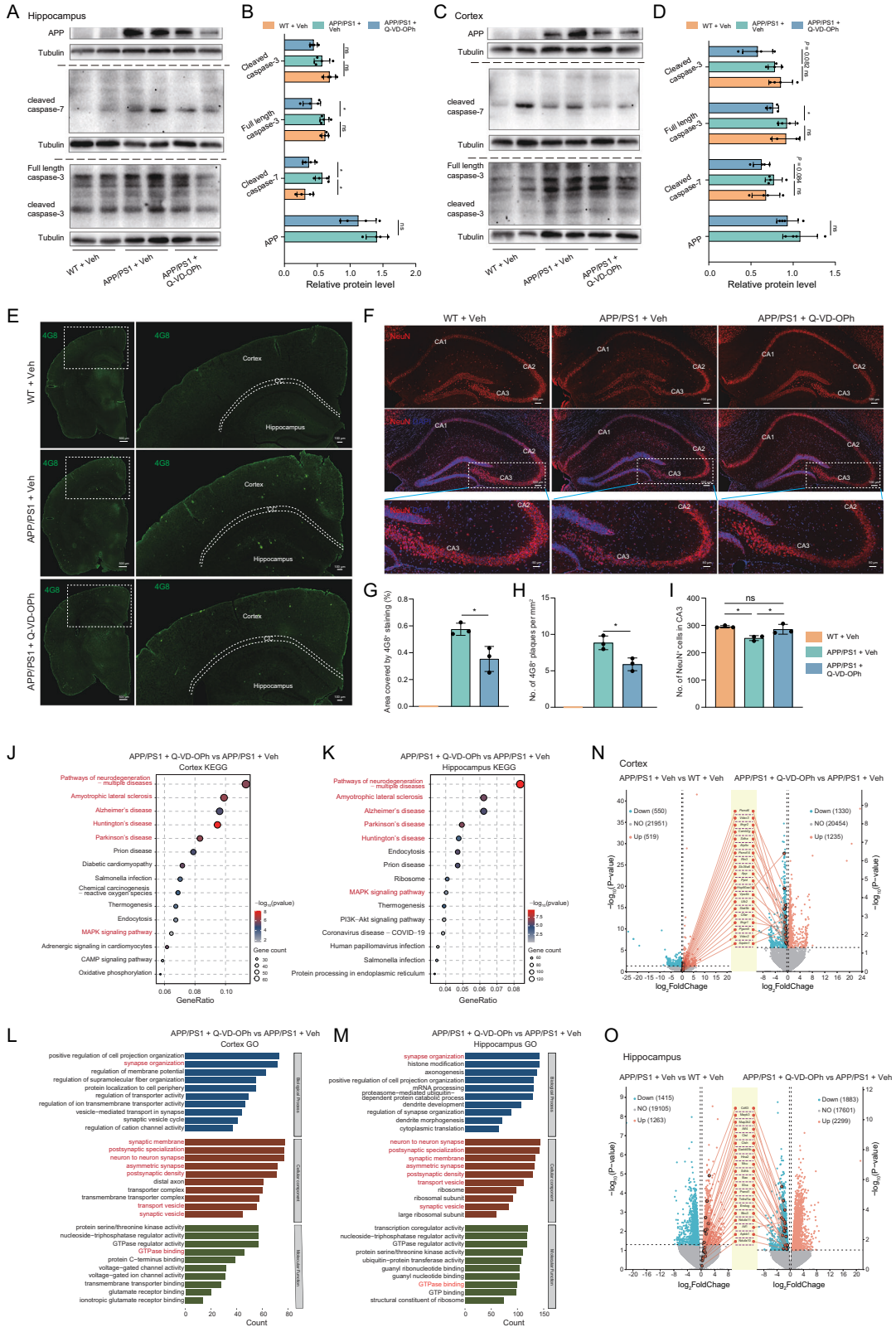

studies have largely focused on individual risk genes or independent variant effects [4–9, 69], we demonstrate that multiple causal genes at 11p11.2 exhibit coordinated downregulation in AD patients and mouse models, and that simultaneous downregulation of *MTCH2*, *NDUFS3*, and *PSMC3* synergistically exacerbates AD pathology via mitochondrial impairment and the caspase-7-mediated apoptosis. This multigenic synergy within a single GWAS locus has been largely overlooked in AD research, and our work (this study and our previous one [13]) thus shifts the paradigm from a "one gene per

Fig. 6 Q-VD-OPh inhibits apoptosis and reduces Aβ plaque deposition in APP/PS1 mice. (A-B) Western blot analysis of APP, caspase-7, and caspase-3 protein levels in the hippocampus of WT and APP/PS1 mice with or without Q-VD-OPh administration for 3 months (A). Protein quantification was performed in four mice per group (WT + Vehicle (Veh), APP/PS1 + Vehicle (Veh), APP/PS1 (AD) + Q-VD-OPh) (B). **(C-D)** Western blot analysis of APP, caspase-7, and caspase-3 protein levels in the cortex (C) and corresponding quantitative analysis (D) using the same cohort as (A-B). **(E)** Representative immunofluorescence images of Aβ plaques in brain tissues using 4G8 antibody (*left*, scale bar = 500 μm; *right*, scale bar = 100 μm). CC, corpus callosum. **(F)** Representative immunofluorescence images of $NeuN^+$ neurons in the hippocampus (*up*, scale bar = 100 μm; *bottom*, scale bar = 50 μm). **(G-H)** Quantification of Aβ plaque burden in the cortex and hippocampus ($n = 3$ mice per group). **(I)** Quantification of $NeuN^+$ cells in the CA3 region of the hippocampus ($n = 3$ mice per group). Each mouse in (G-I) was analyzed across three brain slices, with average value representing the individual animal. **(J-K)** KEGG enrichment analysis of DEGs in the cortex (J) and hippocampus (K) of APP/PS1 mice with and without Q-VD-OPh administration. **(L-M)** GO enrichment analysis of DEGs in cortex (L) and hippocampus (M) of APP/PS1 mice with and without Q-VD-OPh treatment. **(N-O)** Volcano plots depicting DEGs in the cortex (N) and hippocampus (O) of WT and APP/PS1 mice in (A), highlighting AD- and apoptosis-related genes. Values are presented as mean ± SD in (B, D and G-I). Statistical analyses were conducted one-way ANOVA (B, D, I) and two-tailed unpaired *t*-test (G, H); ns, not significant; *, $P < 0.05$.

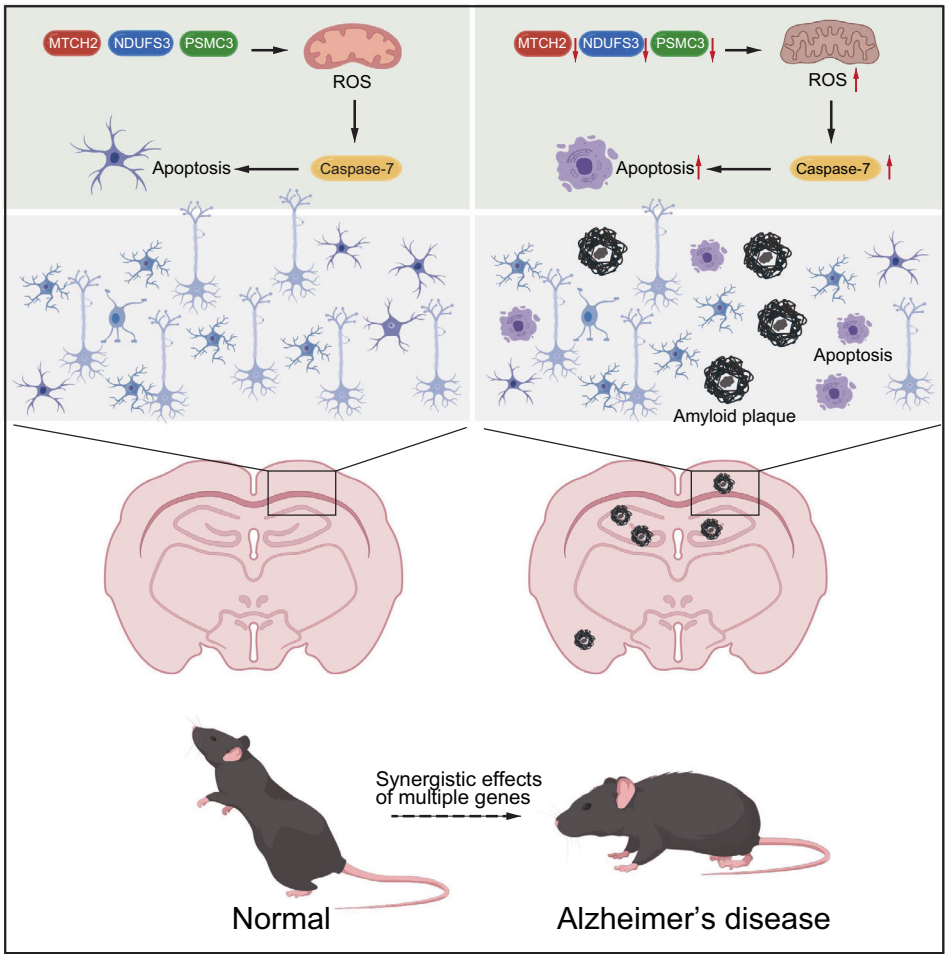

Fig. 7 Proposed mechanism underlying the role of *MTCH2*, *NDUFS3*, and *PSMC3* down-regulation in AD. AD pathogenesis is driven by the cumulative effects of multiple risk genes. Simultaneous down-regulation of *MTCH2*, *NDUFS3*, and *PSMC3* at 11p11.2 leads to increased mROS, which, in turn, promotes caspase-7-mediated apoptosis, thereby exacerbating AD-related phenotypes.

locus" view to a cooperative network model, offering a new framework for dissecting the complex genetic architecture of AD.

Several critical questions remain unresolved: (1) Do specific genes within a synergistic network exert dominant effects, while others play auxiliary roles? In the regulation of apoptosis, *MTCH2*, *NDUFS3*, and *PSMC3* did not contribute equally, with *PSMC3* exhibiting a seemingly stronger effect. Further research is required to determine whether a hierarchical regulatory structure exists among these genes. Moreover, RNA-seq-based synergistic analysis predicted that combined knockdown of *MTCH2*, *NDUFS3*, and *PSMC3* would yield effects greater than the sum of individual perturbations, and our functional validation confirmed that triple knockdown consistently produced more severe mitochondrial and apoptotic phenotypes than any single-gene knockdown. This cooperativity, while not strictly fitting the mathematical definition of synergy, might reflect a biological reality: the simultaneous loss of these three genes pushes cells past a threshold point, leading to disproportionately severe pathological outcomes. (2) How does multigene synergism influence complex AD pathogenesis across different cell types? The current study focused on synergistic gene regulation within a single cell type, yet AD is characterized by complex intercellular interactions across various brain regions. The cell-type-specific expression patterns of these genes and their role in intercellular signaling warrant further investigation.

Neuronal cell death is a hallmark feature of neurodegenerative diseases, including AD [66, 67, 76–78]. Extensive research has

demonstrated a strong association between apoptosis and AD progression, with numerous apoptosis-related proteins, such as Bcl-2, Bax, and caspase-8, exhibiting altered expression patterns in AD patient brains [66, 79–81]. In this study, simultaneous downregulation of *MTCH2*, *NDUFS3*, and *PSMC3* influenced AD development via caspase-7-mediated apoptosis regulation, consistent with reports linking a rare *CASP7* missense variant to familial late-onset AD [63]. Furthermore, alternative processing of APP led to caspase-7-mediated cleavage of the C31 fragment, a potentially neurotoxic APP-derived C-terminal fragment [63, 82, 83]. While the precise role of caspase-7 in AD pathogenesis remains to be determined, targeting apoptosis has been explored as a potential therapeutic strategy. Several apoptosis inhibitors have demonstrated neuroprotective potential in AD models. Humanin, a potent antiapoptotic peptide, inhibits Bax activation [84–87], thereby mitigating Aβ-induced cognitive impairment and inflammatory responses in rodent models [80, 84]. Hesperidin, a citrus-derived flavanone, protects against cognitive deficits by modulating oxidative stress and apoptosis [88]. Similarly, vanillin, a natural phenolic compound, reduces oxidative stress, caspase-3 activity, and Aβ deposition, thereby alleviating AD-like symptoms in aluminum chloride and D-galactose-induced models [89]. In this study, pharmacological inhibition of caspase-7-mediated apoptosis using Q-VD-OPh effectively reduced neuronal apoptosis, decreased amyloid burden, and improved memory function in APP/PS1 mice, further highlighting apoptosis modulation as a potential therapeutic target in AD. Importantly, our results showed that early Q-VD-OPh treatment (in APP/PS mice at 6 months of age) produces sustained behavioral improvement up to 9 months of age. It would be valuable to investigate whether Q-VD-OPh remains effective at later, more advanced stages of pathology (e.g., 9 months of age). This question is clinically relevant, as it addresses the potential for stage-specific therapy in AD and warrants further investigation. Notably, previous studies showed that apoptosis inhibition alone is not sufficient to fully reverse AD-related phenotypes, emphasizing the need for multifactorial treatment strategies [90]. Indeed, advances in genetic epidemiology suggest that targeting multiple disease pathways may offer greater therapeutic potential than single-target approaches [13, 91–93]. Multiple causal genes within the same genetic risk locus often contribute to distinct yet interconnected biological processes. For instance, *MTCH2*, *NDUFS3*, and *PSMC3*, the three causal genes at 11p11.2, are involved in mitochondrial function and proteasomal degradation, both of which are critical for neuronal survival. Coordinated regulation of these genes through shared regulatory elements may enable the simultaneous modulation of multiple cellular functions, providing a potential avenue for mitigating cellular dysfunction in AD. Similarly, Caspase-7 is an effector of mitochondrial apoptosis by activating downstream of mitochondrial outer membrane permeabilization and cytochrome c release [94, 95], and its activation is directly linked to mitochondrial dysfunction in AD pathogenesis.

In short, this study provides direct experimental evidence that synergistic interactions among multiple causal genes (*MTCH2*, *NDUFS3*, and *PSMC3*) at the 11p11.2 locus contribute to AD pathogenesis by disrupting mitochondrial function and promoting apoptosis. Pharmacological inhibition of caspase-7-mediated apoptosis using Q-VD-OPh attenuated neuronal apoptosis, reduced Aβ plaque deposition, and ameliorated memory deficits in APP/PS1 mice. These findings highlight the importance of targeting polygenic synergism in AD therapy and provide novel insights into the complex pathogenic mechanisms underlying neurodegeneration.

DATA AVAILABILITY

All sequencing data analyzed in this study were deposited in the Genome Sequence Archive [96] in National Genomics Data Center [97] under accession number CRA023185 (https://ngdc.cncb.ac.cn/gsa/browse/CRA023185) and HRA010801 (https://ngdc.cncb.ac.cn/gsa-human/browse/HRA010801). All data are available in the manuscript or supplementary materials. Any additional information required to reanalyze the data reported in this paper is available from the lead contact upon reasonable request.

CODE AVAILABILITY

This study did not generate any new algorithms or software. The R scripts used to analyze data and generate figures are available upon request to the corresponding author.

REFERENCES

1. McKhann GM, Knopman DS, Chertkow H, Hyman BT, Jack CR Jr., Kawas CH, et al. The diagnosis of dementia due to Alzheimer's disease: recommendations from the National Institute on Aging-Alzheimer's Association workgroups on diagnostic guidelines for Alzheimer's disease. Alzheimers Dement. 2011;7:263–9.
2. Scheltens P, De Strooper B, Kivipelto M, Holstege H, Chételat G, Teunissen CE, et al. Alzheimer's disease. Lancet. 2021;397:1577–90.
3. Sierksma A, Escott-Price V, De Strooper B. Translating genetic risk of Alzheimer's disease into mechanistic insight and drug targets. Science. 2020;370:61–66.
4. Zhang DF, Xu M, Bi R, Yao YG. Genetic analyses of Alzheimer's disease in China: achievements and perspectives. ACS Chem Neurosci. 2019;10:890–901.
5. Andrews SJ, Fulton-Howard B, Goate A. Interpretation of risk loci from genome-wide association studies of Alzheimer's disease. Lancet Neurol. 2020;19:326–35.
6. Kunkle BW, Grenier-Boley B, Sims R, Bis JC, Damotte V, Naj AC, et al. Genetic meta-analysis of diagnosed Alzheimer's disease identifies new risk loci and implicates Aβ, tau, immunity and lipid processing. Nat Genet. 2019;51:414–30.
7. Jansen IE, Savage JE, Watanabe K, Bryois J, Williams DM, Steinberg S, et al. Genome-wide meta-analysis identifies new loci and functional pathways influencing Alzheimer's disease risk. Nat Genet. 2019;51:404–13.
8. Schwartzentruber J, Cooper S, Liu JZ, Barrio-Hernandez I, Bello E, Kumasaka N, et al. Genome-wide meta-analysis, fine-mapping and integrative prioritization implicate new Alzheimer's disease risk genes. Nat Genet. 2021;53:392–402.
9. Chen S-D, Zhang W, Li Y-Z, Yang L, Huang Y-Y, Deng Y-T, et al. A phenome-wide association and mendelian randomization study for Alzheimer's disease: a prospective cohort study of 502,493 participants from the UK biobank. Biol Psychiatry. 2023;93:790–801.
10. Goate A, Chartierharlin MC, Mullan M, Brown J, Crawford F, Fidani L, et al. Segregation of a missense mutation in the amyloid precursor protein gene with familial Alzheimer's disease. Nature. 1991;349:704–6.
11. Levylahad E, Wasco W, Poorkaj P, Romano DM, Oshima J, Pettingell WH, et al. Candidate gene for the chromosome 1 familial Alzheimer's disease locus. Science. 1995;269:973–7.
12. Sherrington R, Rogaev EI, Liang Y, Rogaeva EA, Levesque G, Ikeda M, et al. Cloning of a gene bearing missense mutations in early-onset familial Alzheimer's disease. Nature. 1995;375:754–60.
13. Xu M, Liu QJ, Bi R, Li Y, Li HL, Kang WB, et al. Coexistence of multiple functional variants and genes underlies genetic risk locus 11p11.2 of Alzheimer's disease. Biol Psychiatry. 2023;94:743–59.
14. Schrode N, Ho SM, Yamamuro K, Dobbyn A, Huckins L, Matos MR, et al. Synergistic effects of common schizophrenia risk variants. Nat Genet. 2019;51:1475–85.
15. Zhang S, Zhang H, Forrest MP, Zhou Y, Sun X, Bagchi VA, et al. Multiple genes in a single GWAS risk locus synergistically mediate aberrant synaptic development and function in human neurons. Cell Genom. 2023;3:100399.
16. Schrode N, Seah C, Deans PJM, Hoffman G, Brennand KJ. Analysis framework and experimental design for evaluating synergy-driving gene expression. Nat Protoc. 2021;16:812–40.
17. Luo R, Su LY, Li G, Yang J, Liu Q, Yang LX, et al. Activation of PPARA-mediated autophagy reduces Alzheimer disease-like pathology and cognitive decline in a murine model. Autophagy. 2020;16:52–69.
18. Jankowsky JL, Fadale DJ, Anderson J, Xu GM, Gonzales V, Jenkins NA, et al. Mutant presenilins specifically elevate the levels of the 42 residue beta-amyloid peptide in vivo: evidence for augmentation of a 42-specific gamma secretase. Hum Mol Genet. 2004;13:159–70.
19. Zhang D-F, Li J, Wu H, Cui Y, Bi R, Zhou H-J, et al. CFH variants affect structural and functional brain changes and genetic risk of Alzheimer's disease. Neuropsychopharmacology. 2015;41:1034–45.
20. Chen A, Liao S, Cheng M, Ma K, Wu L, Lai Y, et al. Spatiotemporal transcriptomic atlas of mouse organogenesis using DNA nanoball-patterned arrays. Cell. 2022;185:1777–1792.e1721.
21. Wolf FA, Angerer P, Theis FJ. SCANPY: large-scale single-cell gene expression data analysis. Genome Biol. 2018;19:15.

22. Yao Z, van Velthoven CTJ, Kunst M, Zhang M, McMillen D, Lee C, et al. A high-resolution transcriptomic and spatial atlas of cell types in the whole mouse brain. Nature. 2023;624:317–32.
23. Schindelin J, Arganda-Carreras I, Frise E, Kaynig V, Longair M, Pietzsch T, et al. Fiji: an open-source platform for biological-image analysis. Nat Methods. 2012;9:676–82.
24. Luo R, Fan Y, Yang J, Ye M, Zhang DF, Guo K, et al. A novel missense variant in ACAA1 contributes to early-onset Alzheimer's disease, impairs lysosomal function, and facilitates amyloid-beta pathology and cognitive decline. Signal Transduct Target Ther. 2021;6:325.
25. Xu L, Yu D, Xu M, Liu Y, Yang LX, Zou QC, et al. Primate-specific BTN3A2 protects against SARS-CoV-2 infection by interacting with and reducing ACE2. EBioMedicine. 2024;107:105281.
26. Liu X, Jin Y, Wan X, Liang X, Wang K, Liu J, et al. SALIS transcriptionally represses IGFBP3/Caspase-7-mediated apoptosis by associating with STAT5A to promote hepatocellular carcinoma. Cell Death Dis. 2022;13:642.
27. Jiang H-Y, Yang Y, Zhang Y-Y, Xie Z, Zhao X-Y, Sun Y, et al. The dual role of poly(ADP-ribose) polymerase-1 in modulating parthanatos and autophagy under oxidative stress in rat cochlear marginal cells of the stria vascularis. Redox Biol. 2018;14:361–70.
28. Yu J, Xiao K, Chen X, Deng L, Zhang L, Li Y, et al. Neuron-derived neuropeptide Y fine-tunes the splenic immune responses. Neuron. 2022;110:1327–1339 e1326.
29. Xu M, Zhang DF, Luo R, Wu Y, Zhou H, Kong LL, et al. A systematic integrated analysis of brain expression profiles reveals YAP1 and other prioritized hub genes as important upstream regulators in Alzheimer's disease. Alzheimers Dement. 2017;14:215–29.
30. Chen S. Ultrafast one-pass FASTQ data preprocessing, quality control, and deduplication using fastp. Imeta. 2023;2:e107.
31. Kim D, Langmead B, Salzberg SL. HISAT: a fast spliced aligner with low memory requirements. Nat Methods. 2015;12:357–60.
32. Dobin A, Davis CA, Schlesinger F, Drenkow J, Zaleski C, Jha S, et al. STAR: ultrafast universal RNA-seq aligner. Bioinformatics. 2013;29:15–21.
33. Pertea M, Kim D, Pertea GM, Leek JT, Salzberg SL. Transcript-level expression analysis of RNA-seq experiments with HISAT, StringTie and Ballgown. Nat Protoc. 2016;11:1650–67.
34. Li B, Dewey CN. RSEM: accurate transcript quantification from RNA-Seq data with or without a reference genome. BMC Bioinformatics. 2011;12:323.
35. Yu G, Wang LG, Han Y, He QY. clusterProfiler: an R package for comparing biological themes among gene clusters. OMICS. 2012;16:284–7.
36. Wu T, Hu E, Xu S, Chen M, Guo P, Dai Z, et al. clusterProfiler 4.0: A universal enrichment tool for interpreting omics data. The Innovation. 2021;2:100141.
37. van Oostrum M, Blok TM, Giandomenico SL, tom Dieck S, Tushev G, Fürst N, et al. The proteomic landscape of synaptic diversity across brain regions and cell types. Cell. 2023;186:5411–5427.e5423.
38. Jiang S, Li H, Zhang L, Mu W, Zhang Y, Chen T, et al. Generic Diagramming Platform (GDP): a comprehensive database of high-quality biomedical graphics. Nucleic Acids Res. 2025;53:D1670–D1676.
39. Rohn TT, Kokoulina P, Eaton CR, Poon WW. Caspase activation in transgenic mice with Alzheimer-like pathology: results from a pilot study utilizing the caspase inhibitor, Q-VD-OPh. Int J Clin Exp Med. 2009;2:300–8.
40. Laforge M, Silvestre R, Rodrigues V, Garibal J, Campillo-Gimenez L, Mouhamad S, et al. The anti-caspase inhibitor Q-VD-OPH prevents AIDS disease progression in SIV-infected rhesus macaques. J Clin Invest. 2018;128:1627–40.
41. Martorell AJ, Paulson AL, Suk HJ, Abdurrob F, Drummond GT, Guan W, et al. Multi-sensory gamma stimulation ameliorates Alzheimer's-associated pathology and improves cognition. Cell. 2019;177:256–271 e222.
42. Mathys H, Peng Z, Boix CA, Victor MB, Leary N, Babu S, et al. Single-cell atlas reveals correlates of high cognitive function, dementia, and resilience to Alzheimer's disease pathology. Cell. 2023;186:4365–4385.e4327.
43. Mathys H, Boix CA, Akay LA, Xia Z, Davila-Velderrain J, Ng AP, et al. Single-cell multiregion dissection of Alzheimer's disease. Nature. 2024;632:858–68.
44. Matarin M, Salih Dervis A, Yasvoina M, Cummings Damian M, Guelfi S, Liu W, et al. A genome-wide gene-expression analysis and database in transgenic mice during development of amyloid or tau pathology. Cell Rep. 2015;10:633–44.
45. Song M, Yang X, Ren X, Maliskova L, Li B, Jones IR, et al. Mapping cis-regulatory chromatin contacts in neural cells links neuropsychiatric disorder risk variants to target genes. Nat Genet. 2019;51:1252–62.
46. Nott A, Holtman IR, Coufal NG, Schlachetzki JCM, Yu M, Hu R, et al. Brain cell type-specific enhancer-promoter interactome maps and disease-risk association. Science. 2019;366:1134–9.
47. Peralta S, Pinto M, Arguello T, Garcia S, Diaz F, Moraes CT. Metformin delays neurological symptom onset in a mouse model of neuronal complex I deficiency. JCI Insight. 2020;5:e141183.
48. Kröll-Hermi A, Ebstein F, Stoetzel C, Geoffroy V, Schaefer E, Scheidecker S, et al. Proteasome subunit PSMC3 variants cause neurosensory syndrome combining deafness and cataract due to proteotoxic stress. EMBO Mol Med. 2020;12:e11861.
49. Rahman J, Rahman S. Mitochondrial medicine in the omics era. The Lancet. 2018;391:2560–74.
50. Concannon CG, Koehler BF, Reimertz C, Murphy BM, Bonner C, Thurow N, et al. Apoptosis induced by proteasome inhibition in cancer cells: predominant role of the p53/PUMA pathway. Oncogene. 2007;26:1681–92.
51. Jiang S, Srikanth M, Serpe R, Yavari S, Gaur P, Collins GA, et al. Early proteasome downregulation and dysfunction drive proteostasis failure in Alzheimer's disease. Brain. 2025;148:4372–88.
52. Church TR, Margolis SS. Mechanisms of ubiquitin-independent proteasomal degradation and their roles in age-related neurodegenerative disease. Front Cell Dev Biol. 2024;12:1531797.
53. Mannan A, Sharma A, Singh TG. Boosting brain clean-up: can targeting UPS genes offer neuroprotection? Mol Neurobiol. 2025;62:16512–56.
54. Ai YW, Meng YT, Yan B, Zhou QY, Wang XD. The biochemical pathways of apoptotic, necroptotic, pyroptotic, and ferroptotic cell death. Mol Cell. 2024;84:170–9.
55. Lamkanfi M, Kanneganti T-D. Caspase-7: A protease involved in apoptosis and inflammation. Int J Biochem Cell Biol. 2010;42:21–24.
56. Jin Z, Wei W, Yang M, Du Y, Wan Y. Mitochondrial complex I activity suppresses inflammation and enhances bone resorption by shifting macrophage-osteoclast polarization. Cell Metab. 2014;20:483–98.
57. Wu H, Wang YQ, Ying MF, Jin CM, Li JT, Hu X. Lactate dehydrogenases amplify reactive oxygen species in cancer cells in response to oxidative stimuli. Signal Transduct Target Ther. 2021;6:242.
58. Cillero-Pastor B, Caramés B, Lires-Deán M, Vaamonde-García C, Blanco FJ, López-Armada MJ. Mitochondrial dysfunction activates cyclooxygenase 2 expression in cultured normal human chondrocytes. Arthritis Rheum. 2008;58:2409–19.
59. Zhu H-L, Shi X-T, Xu X-F, Zhou G-X, Xiong Y-W, Yi S-J, et al. Melatonin protects against environmental stress-induced fetal growth restriction via suppressing ROS-mediated GCN2/ATF4/BNIP3-dependent mitophagy in placental trophoblasts. Redox Biol. 2021;40:101854.
60. Xu S-C, He M-D, Lu Y-H, Li L, Zhong M, Zhang Y-W, et al. Nickel exposure induces oxidative damage to mitochondrial DNA in Neuro2a cells: the neuroprotective roles of melatonin. J Pineal Res. 2011;51:426–33.
61. Pi H, Xu S, Reiter RJ, Guo P, Zhang L, Li Y, et al. SIRT3-SOD2-mROS-dependent autophagy in cadmium-induced hepatotoxicity and salvage by melatonin. Autophagy. 2015;11:1037–51.
62. Li N, Ragheb K, Lawler G, Sturgis J, Rajwa B, Melendez JA, et al. Mitochondrial complex I inhibitor rotenone induces apoptosis through enhancing mitochondrial reactive oxygen species production. J Biol Chem. 2003;278:8516–25.
63. Zhang X, Zhu C, Beecham G, Vardarajan BN, Ma Y, Lancour D, et al. A rare missense variant of CASP7 is associated with familial late-onset Alzheimer's disease. Alzheimers Dement. 2018;15:441–52.
64. Fu J, Lai X, Zhang C, Wei Q, Chen X, Shang H. Correlation analysis of peripheral platelet markers and disease phenotypes in Alzheimer's disease. Alzheimers Dement. 2024;20:4366–72.
65. Wu Q, Wang W, Huang Z, Lin X, Yao M, Cai C, et al. Unveiling the molecular mechanisms of Danggui-Shaoyao-San against Alzheimer's disease in APP/PS1 mice via integrating proteomic and metabolomic approaches. Alzheimers Res Ther. 2024;16:251.
66. Ekundayo BE, Obafemi TO, Adewale OB, Obafemi BA, Oyinloye BE, Ekundayo SK. Oxidative stress, endoplasmic reticulum stress and apoptosis in the pathology of Alzheimer's disease. Cell Biochem Biophys. 2024;82:457–77.
67. Chi H, Chang H-Y, Sang T-K. Neuronal cell death mechanisms in major neurodegenerative diseases. Int J Mol Sci. 2018;19:3082.
68. Li Y, Xu M, Xiang B, Li X, Zhang D, Zhao H, et al. Functional genomics identify causal variant underlying the protective CTSH locus for Alzheimer's disease. Neuropsychopharmacology. 2023;48:1555–66.
69. Andrews SJ, Renton AE, Fulton-Howard B, Podlesny-Drabiniok A, Marcora E, Goate AM. The complex genetic architecture of Alzheimer's disease: novel insights and future directions. EBioMedicine. 2023;90:104511.
70. Mullan M, Crawford F, Axelman K, Houlden H, Lilius L, Winblad B, et al. A pathogenic mutation for probable Alzheimer's disease in the APP gene at the N-terminus of beta-amyloid. Nat Genet. 1992;1:345–7.
71. Cruts M, Backhovens H, Wang SY, Van Gassen G, Theuns J, De Jonghe CD, et al. Molecular genetic analysis of familial early-onset Alzheimer's disease linked to chromosome 14q24.3. Hum Mol Genet. 1995;4:2363–71.
72. Rogaev EI, Sherrington R, Rogaeva EA, Levesque G, Ikeda M, Liang Y, et al. Familial Alzheimer's disease in kindreds with missense mutations in a gene on chromosome 1 related to the Alzheimer's disease type 3 gene. Nature. 1995;376:775–8.
73. Bertram L, Tanzi RE. Thirty years of Alzheimer's disease genetics: the implications of systematic meta-analyses. Nat Rev Neurosci. 2008;9:768–78.
74. Guerreiro RJ, Gustafson DR, Hardy J. The genetic architecture of Alzheimer's disease: beyond APP, PSENs and APOE. Neurobiol Aging. 2012;33:437–56.

75. Harvey RJ, Rossor MN. Does early-onset Alzheimer disease constitute a distinct subtype? The contribution of molecular genetics. Alzheimer Dis Assoc Disord. 1995; **9 Suppl 1** :S7–S13.
76. Kim TA, Syty MD, Wu K, Ge S. Adult hippocampal neurogenesis and its impairment in Alzheimer's disease. Zool Res. 2022;43:481–96.
77. Li Y, Xu N-N, Hao Z-Z, Liu S. Adult neurogenesis in the primate hippocampus. Zool Res. 2023;44:315–22.
78. Balusu S, De Strooper B. The necroptosis cell death pathway drives neurodegeneration in Alzheimer's disease. Acta Neuropathol. 2024;147:96.
79. Callens M, Kraskovskaya N, Derevtsova K, Annaert W, Bultynck G, Bezprozvanny I, et al. The role of Bcl-2 proteins in modulating neuronal Ca2+ signaling in health and in Alzheimer's disease. Biochim Biophys Acta Mol Cell Res. 2021;1868:118997.
80. Obulesu M, Lakshmi MJ. Apoptosis in Alzheimer's disease: an understanding of the physiology, pathology and therapeutic avenues. Neurochem Res. 2014;39:2301–12.
81. Wang X-J, Cao Q, Zhang Y, Su X-D. Activation and regulation of Caspase-6 and its role in neurodegenerative diseases. Annu Rev Pharmacol Toxicol. 2015;55:553–72.
82. Kline AE, Fiorelli T, Kirouac L, Padmanabhan J. Altered processing of amyloid precursor protein in cells undergoing apoptosis. PLoS ONE. 2013;8:e57979.
83. Nhan HS, Chiang K, Koo EH. The multifaceted nature of amyloid precursor protein and its proteolytic fragments: friends and foes. Acta Neuropathol. 2014;129:1–19.
84. Zapała, Kaczyński B, Kieć-Wilk B, Staszel T, Knapp A, Hege Thoresen G, et al. Humanins, the neuroprotective and cytoprotective peptides with antiapoptotic and anti-inflammatory properties. Pharmacol Rep. 2010;62:767–77.
85. Luciano F, Zhai D, Zhu X, Bailly-Maitre B, Ricci J-E, Satterthwait AC, et al. Cytoprotective peptide humanin binds and inhibits proapoptotic Bcl-2/Bax family protein BimEL. J Biol Chem. 2005;280:15825–35.
86. Kariya S, Hirano M, Nagai Y, Furiya Y, Fujikake N, Toda T, et al. Humanin attenuates apoptosis induced by DRPLA proteins with expanded polyglutamine stretches. J Mol Neurosci. 2003;25:165–9.
87. Sponne I, Fifre A, Koziel V, Kriem B, Oster T, Pillot T. Humanin rescues cortical neurons from prion-peptide-induced apoptosis. Mol Cell Neurosci. 2004;25:95–102.
88. Justin Thenmozhi A, William Raja TR, Manivasagam T, Janakiraman U, Essa MM. Hesperidin ameliorates cognitive dysfunction, oxidative stress and apoptosis against aluminium chloride induced rat model of Alzheimer's disease. Nutr Neurosci. 2016;20:360–8.
89. Anand A, Khurana N, Kaur S, Ali N, AlAsmari AF, Waseem M, et al. The multifactorial role of vanillin in amelioration of aluminium chloride and D-galactose induced Alzheimer's disease in mice. Eur J Pharmacol. 2023;954:175832.
90. Ji D, Zhang J, Liang J, Huang ZS, Shu B, Li D. Efficient strategy for alleviating neuronal apoptosis and oxidative stress damage of Alzheimer's disease through dual targeting BCL-2 gene promoter i-motif and beta-amyloid. Redox Biol. 2025;82:103600.
91. Turgutalp B, Kizil C. Multi-target drugs for Alzheimer's disease. Trends Pharmacol Sci. 2024;45:628–38.
92. Reitz C, Pericak-Vance MA, Foroud T, Mayeux R. A global view of the genetic basis of Alzheimer disease. Nat Rev Neurol. 2023;19:261–77.
93. Bellenguez C, Küçükali F, Jansen IE, Kleineidam L, Moreno-Grau S, Amin N, et al. New insights into the genetic etiology of Alzheimer's disease and related dementias. Nat Genet. 2022;54:412–36.
94. Lakhani SA, Masud A, Kuida K, Porter GA Jr., Booth CJ, Mehal WZ, et al. Caspases 3 and 7: key mediators of mitochondrial events of apoptosis. Science. 2006;311:847–51.
95. Chandler JM, Cohen GM, MacFarlane M. Different subcellular distribution of caspase-3 and caspase-7 following Fas-induced apoptosis in mouse liver. J Biol Chem. 1998;273:10815–8.
96. Chen T, Chen X, Zhang S, Zhu J, Tang B, Wang A, et al. The genome sequence archive family: toward explosive data growth and diverse data types. Genomics Insights. 2021;19:578–83.
97. Bai X, Bao Y, Bei S, Bu C, Cao R, Cao Y, et al. Database resources of the national genomics data center, china national center for bioinformation in 2024. Nucleic Acids Res. 2024;52:D18–D32.
98. Kang HJ, Kawasawa YI, Cheng F, Zhu Y, Xu X, Li M, et al. Spatio-temporal transcriptome of the human brain. Nature. 2011;478:483–9.

ACKNOWLEDGEMENTS

We thank the Institutional Center for Shared Technologies and Facilities of Kunming Institute of Zoology, Chinese Academy of Sciences, for providing confocal microscopy images and flow cytometry analysis. We thank Zhiyu Ma and Cong Li for technical support. We thank the staff members of the National Research Facility for Phenotypic & Genetic Analysis of Model Animals (Primate Facility) (https://cstr.cn/31137.02.NPRC), for providing technical support and assistance in data collection and analysis.

AUTHOR CONTRIBUTIONS

Y.-G.Y. conceived and designed the study; J.-S.Y. performed all the experiments with the help of X.-R.W., W.-Y. Z., and Q.-J. L.; J.-S.Y., M.X., and W.-B.K. analyzed all data with the guidance of Y.-G.Y. and D.-F.Z.; J.-S.Y. and Y.-G.Y. wrote the manuscript. All authors read and approved the manuscript.

FUNDING

This work was funded by the National Natural Science Foundation of China (32230021 [to Y.-G.Y.] and 32300826 [to J.-S.Y.]), China Postdoctoral Science Foundation (2024M763353 and GZC20251866 [to J.-S.Y.]), and Yunnan Province (202305AH340006 [to Y.-G.Y.], 202301AT070284 and XDYC-QNRC-2024536 [to J.-S.Y.], 202301AW070013 [to Q-J.L.], and 202401AW070010 [to M.X.]).

COMPETING INTERESTS

The authors declare no competing interests.

ETHICS APPROVAL FOR ANIMAL STUDIES

All methods performed in this study were conducted in accordance with the relevant guidelines and regulations. Ethical approval was obtained from the Institutional Animal Care and Use Committee of Kunming Institute of Zoology, Chinese Academy of Sciences.

ADDITIONAL INFORMATION

Supplementary information The online version contains supplementary material available at https://doi.org/10.1038/s41380-026-03664-7.

Correspondence and requests for materials should be addressed to Yong-Gang Yao.

Reprints and permission information is available at http://www.nature.com/reprints

Publisher's note Springer Nature remains neutral with regard to jurisdictional claims in published maps and institutional affiliations.

Supplemental information

Convergent mitochondrial impairment and apoptosis driven by simultaneous down-regulation of multiple genes at 11p11.2 in Alzheimer's disease

Jinsong Yu, Min Xu, Xiaorong Wu, Wei-Bo Kang, Wei-Yin Zou, Qianjin Liu, Deng-Feng Zhang, Yong-Gang Yao

This supplement contains:
Supplementary Figures and Legends
Supplementary Tables

Supplementary Figures and Legends

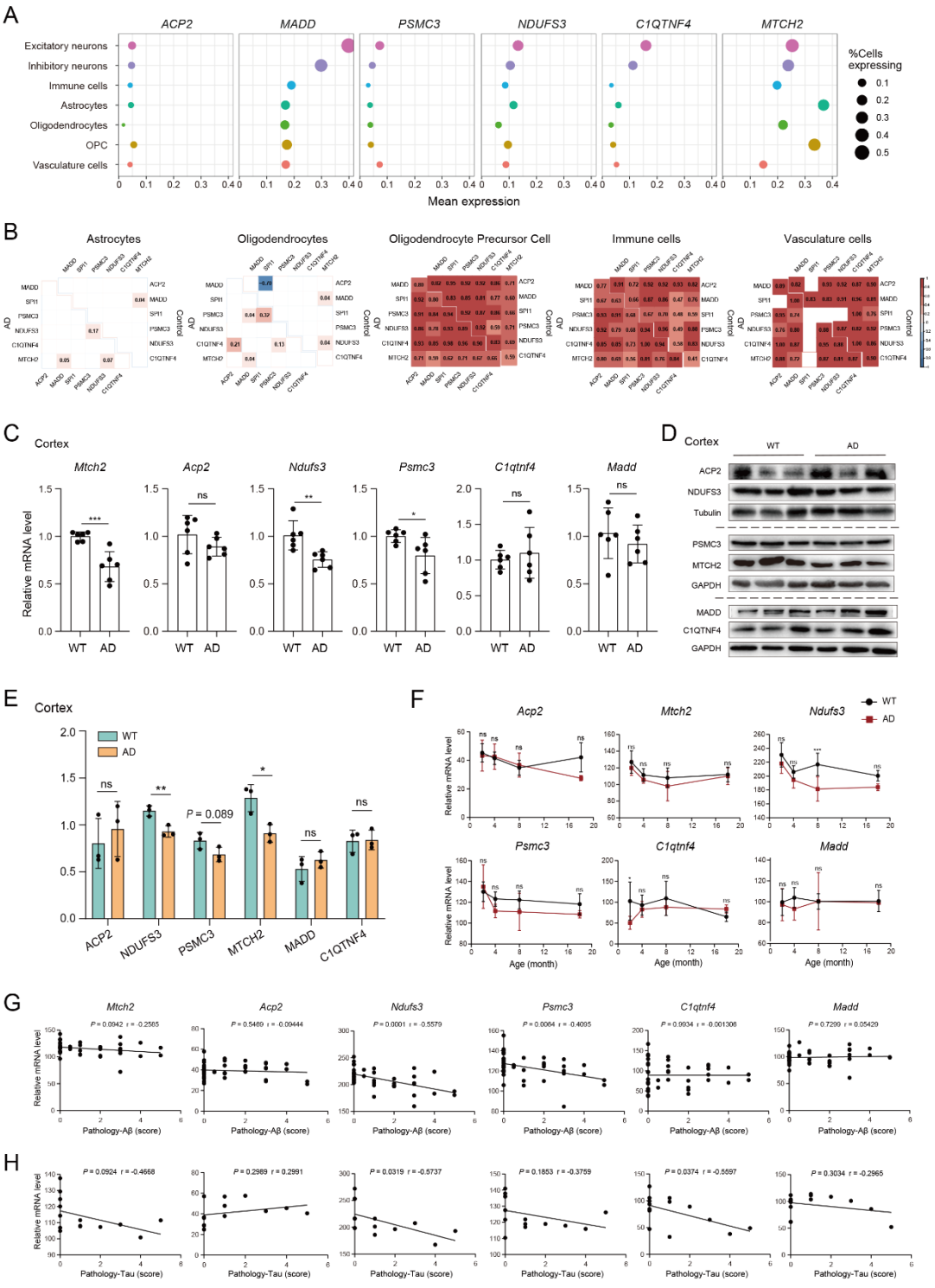

Supplementary Figure 1. Expression changes in six causal genes at the 11p11.2 locus in AD and their correlation with AD-related pathology.

(A) Expression profiles of six causal genes at 11p11.2 across different brain cell types in AD patients, based on publicly available single-cell datasets [1].

(**B**) Correlation analysis of the expression of the six causal genes in multiple cell types

from healthy individuals and AD patients.
(C) Relative mRNA expression levels of six causal genes in the cortex of WT and APP/PS1 mice, quantified by qRT-PCR (WT: $n = 3$; AD: $n = 3$). Data are presented as mean ± standard deviation (SD), analyzed using two-tailed unpaired *t*-test; ns, not significant; *, $P < 0.05$.
(D-E) Protein levels of six causal genes at 11p11.2 in the cortex of WT and APP/PS1 mice (D) and corresponding quantitative analysis (E) (WT: $n = 3$; AD: $n = 3$). Data are presented as mean ± SD, quantified by two-tailed unpaired *t*-test; ns, not significant; *, $P < 0.05$, **, $P < 0.01$.
(F) Relative mRNA expression of six causal genes at 11p11.2 in brain tissues of WT and homozygous TASTPM mice at different ages (2 months, WT, $n = 8$, TASTPM, $n = 4$; 4 months, WT, $n = 7$, TASTPM, $n = 4$; 8 months, WT, $n = 8$, TASTPM, $n = 4$; 18 months, WT, $n = 7$, TASTPM, $n = 2$), based on MouseAC dataset [2]. Values are presented as mean ± SD, quantified by two-way ANOVA with Sidak's multiple comparisons test; ns, not significant; *, $P < 0.05$; ***, $P < 0.001$.
(G-H) Correlation between mRNA levels of six causal genes and Aβ pathology (G) or Tau pathology (H) in AD mice. Original data for mRNA levels and Aβ pathology were obtained from APP mutant mice (13 homozygous $APP^{k670N/M671L}$, 14 homozygous $APP^{k670N/M671L}$-$PSEN1^{M146V}$, 16 heterozygous $APP^{k670N/M671L}$-$PSEN1^{M146V}$ mutant mice), while data for mRNA levels and Tau pathology (14 $MAPT^{P301L}$ mutant mice) were retrieved from the MouseAC dataset [2]. Pearson's correlation test was used for statistical analysis.

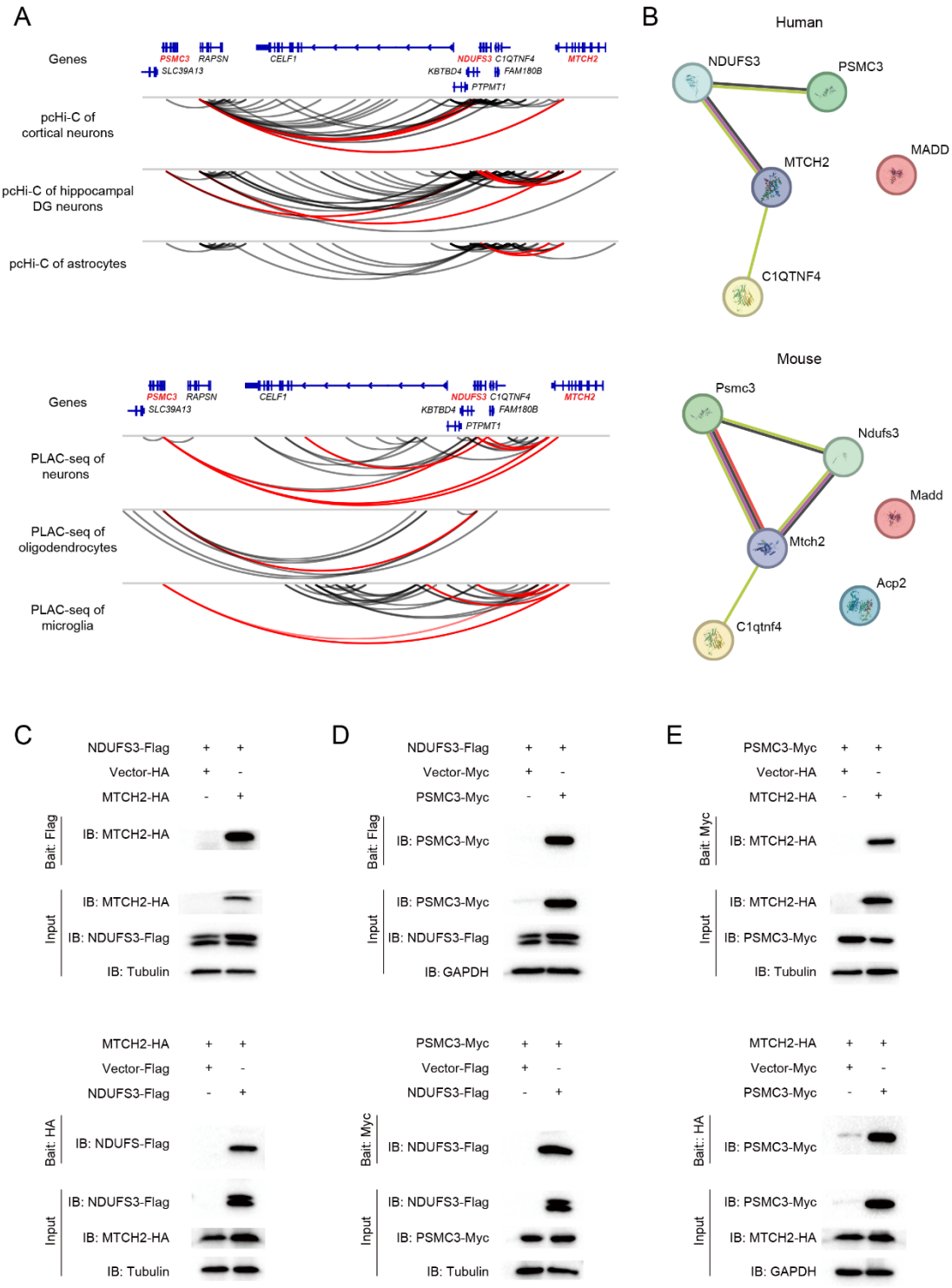

Supplementary Figure 2. Integrated interaction analyses of MTCH2, NDUFS3, and PSMC3.

(A) Promoter capture Hi-C (pcHi-C, upper panel) and proximity ligation-assisted ChiP-seq (PLAC-seq, lower panel) showing interactions among *MTCH2*, *NDUFS3*, and *PSMC3*. The pcHi-C data of iPSC-derived hippocampal DG-like neurons, iPSC-induced cortical excitatory neurons, and human primary fetal astrocytes were downloaded from the GEO database with accession number GSE113481 [3].

Proximity ligation-assisted ChiP-seq (PLAC-seq, lower panel) data [4] of microglia, neurons and oligodendrocytes were obtained from the UCSC (https://genome.ucsc.edu/s/nottalexi/glassLab_BrainCellTypes_hg19). Interactions with score > 5 (corresponded to $P < 1 \times 10^{-5}$) were retained. Interactions among *MTCH2*, *NDUFS3*, and *PSMC3* were highlighted in red.

(B) Protein-Protein interaction (PPI) network for MTCH2, NDUFS3, PSMC3, ACP2, MADD, and C1QTNF4. The PPI network was generated using the online analysis tool STRING (https://string-db.org/) with default parameters.

(C-E) Co-immunoprecipitation (Co-IP) assays validating pairwise interactions among MTCH2, NDUFS3, and PSMC3. Whole-cell lysates were immunoprecipitated with the indicated antibodies.

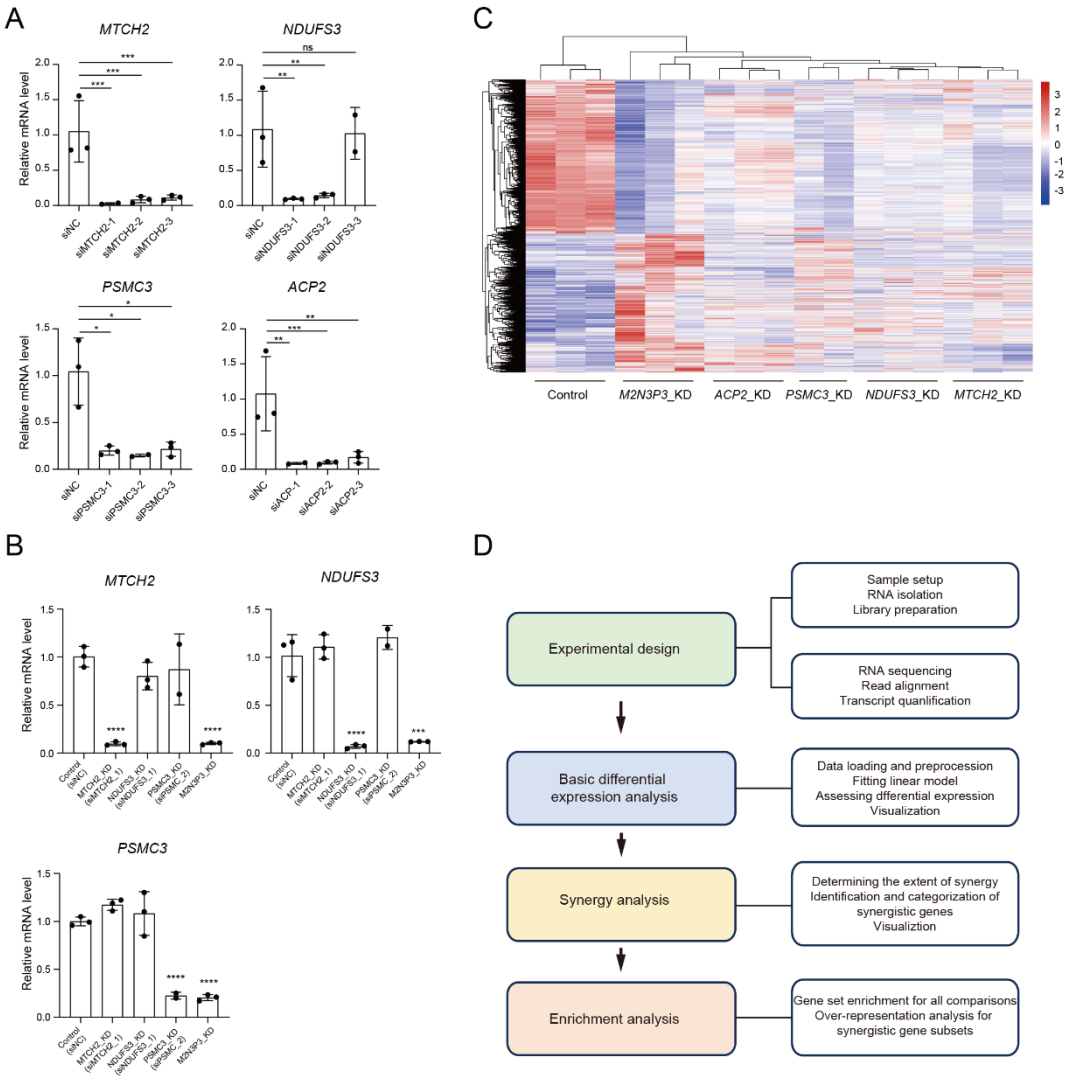

Supplementary Figure 3. Individual or triple gene knockdown of *MTCH2*, *NDUFS3*, *PSMC3*, and *ACP2* using siRNAs.

(A) Comparison of knockdown efficiency of three siRNAs for *MTCH2* (siMTCH2), *NDUFS3* (siNDUFS3), *PSMC3* (siPSMC3), and *ACP2* (siACP2). siMTCH2-1, siNDUFS3-1, siPSMC3-2, and siACP2-1 were selected for subsequent experiments (siNC: $n = 3$; siMTCH2-1: $n = 2$; siMTCH2-2: $n = 3$; siMTCH2-3: $n = 3$; siNDUFS3-1: $n = 3$; siNDUFS3-2: $n = 3$; siNDUFS3-3: $n = 2$; siPSMC3-1: $n = 3$; siPSMC3-2: $n = 2$; siPSMC3-3: $n = 3$; siACP2-1: $n = 2$; siACP2-2: $n = 3$; siACP2-3: $n = 3$). siNC: U251-APP cells transfected with control siRNA.

(B) Efficiency of individual knockdown of *MTCH2* (MTCH2_KD), *NDUFS3* (NDUFS3_KD), and *PSMC3* (PSMC3_KD), or triple gene knockdown (M2N3P3_KD) using siRNA (Control (siNC): $n = 3$; MTCH2_KD: $n = 3$; NDUFS3_KD: $n = 3$; PSMC3_KD: $n = 2$; M2N3P3_KD: $n = 3$). Data in (**A-B**) are presented as mean ± SD, quantified by one-way ANOVA; ns, not significant; *, $P < 0.05$, **, $P < 0.01$, ***, $P < 0.001$, ****, $P < 0.0001$.

(C) RNA-seq heatmap of individual or combined knockdown of *MTCH2*, *NDUFS3*,

and *PSMC3*.
(D) Workflow for assessing synergistic interactions among *MTCH2*, *NDUFS3*, and *PSMC3* (adapted from [5]).

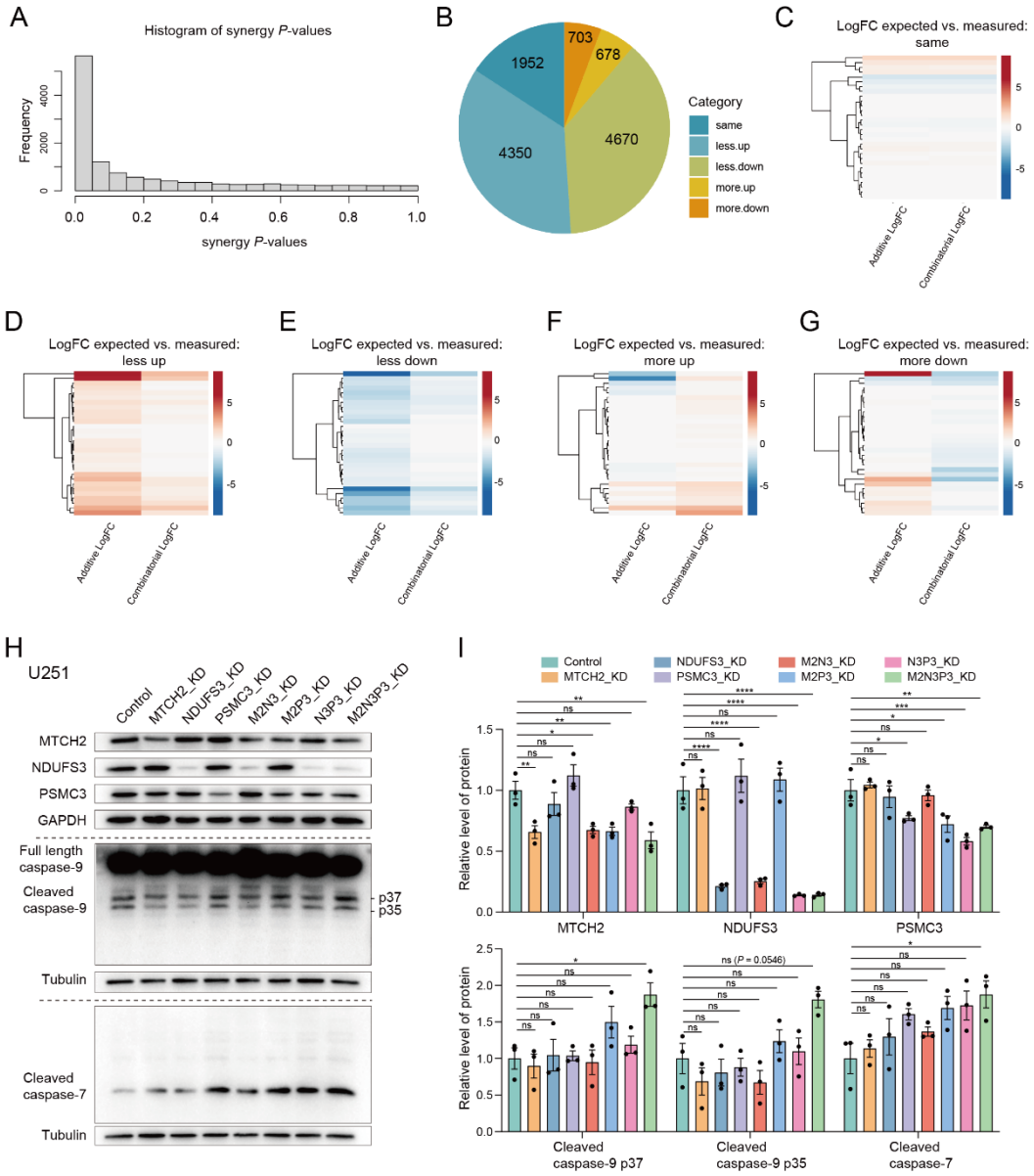

Supplementary Figure 4. Supplementary analyses of synergy-driven gene expression regulation.

(A) Histogram displaying distribution of *P*-values along with corresponding statistical data.

(B) Pie chart illustrating the number and proportion of genes classified into each synergistic category in the combinatorial model compared to the additive model.

(C-G) Differentially expressed values (in $\log_2$FC) and hierarchical clustering across all synergistic categories, comparing the additive model to the combinatorial perturbation model.

(**H-I**) Protein expression levels of caspase-7, caspase-9, MTCH2, NDUFS3, and PSMC3 in U251-APP cells following individual knockdown of *MTCH2* (MTCH2_KD), *NDUFS3* (NDUFS3_KD), and *PSMC3* (PSMC3_KD), pairwise knockdown of 2 of three genes (*MTCH2* and *NDUFS3* knockdown, M2N3_KD;

MTCH2 and *PSMC3* knockdown, M2P3_KD; *NDUFS3* and *PSMC3* knockdown, N3P3_KD), or triple gene knockdown (M2N3P3_KD) (**H**) and corresponding quantitation (**I**) ($n = 3$ per group). Values are presented as mean ± SD. Statistical significance was determined using one-way ANOVA (I); ns, not significant; *, $P < 0.05$; **, $P < 0.01$; ***, $P < 0.001$; ****, $P < 0.0001$.

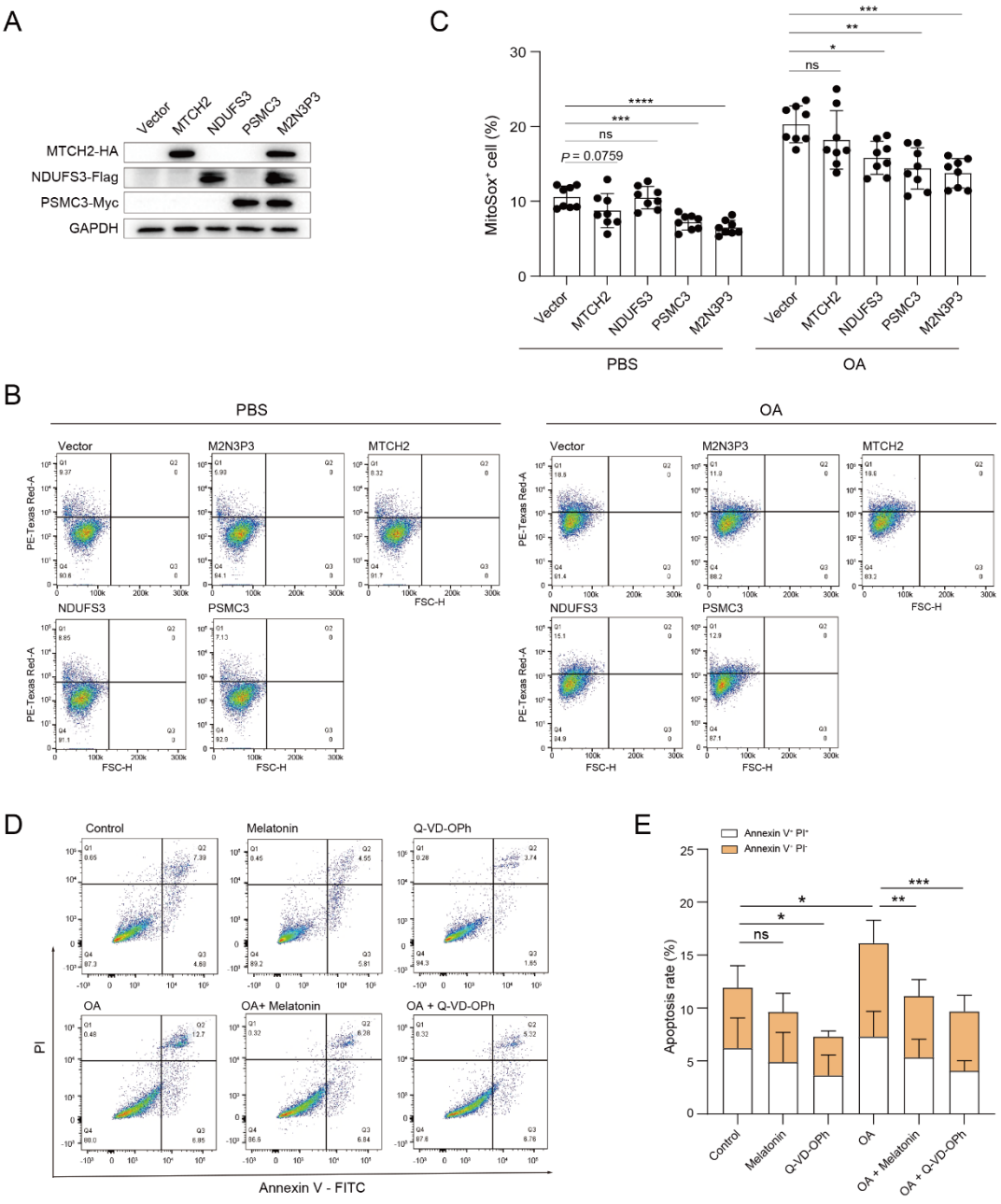

Supplementary Figure 5. Regulation of mROS by *MTCH2*, *NDUFS3*, and *PSMC3*.

(A) Western blotting for U251-APP cell lysates showing the efficiency of individual overexpression of *MTCH2*, *NDUFS3*, and *PSMC3* and triple gene overexpression (M2N3P3).

(B) Representative flow cytometry plots of MitoSOX staining in U251-APP cells following individual overexpression of *MTCH2*, *NDUFS3*, and *PSMC3*, and triple gene overexpression (M2N3P3). Transfected cells were treated with and without OA.

(C) Quantification of MitoSOX^{+} cells from (**B**) (n = 8 per group).

(D) Flow cytometry analysis of U251-APP cells following melatonin, Q-VD-OPh, or OA treatment. Cells were double-stained with Annexin V and propidium iodide (PI).

Cells undergoing early and late apoptosis were defined as Annexin V^+ PI^- and Annexin V^+ PI^+, respectively.
(E) Bar charts showing quantification of apoptosis rate (n = 6 per group).
Data are presented as mean ± SD, quantified by one-way ANOVA (C and E); ns, not significant; *, $P < 0.05$, **, $P < 0.01$, ***, $P < 0.001$.

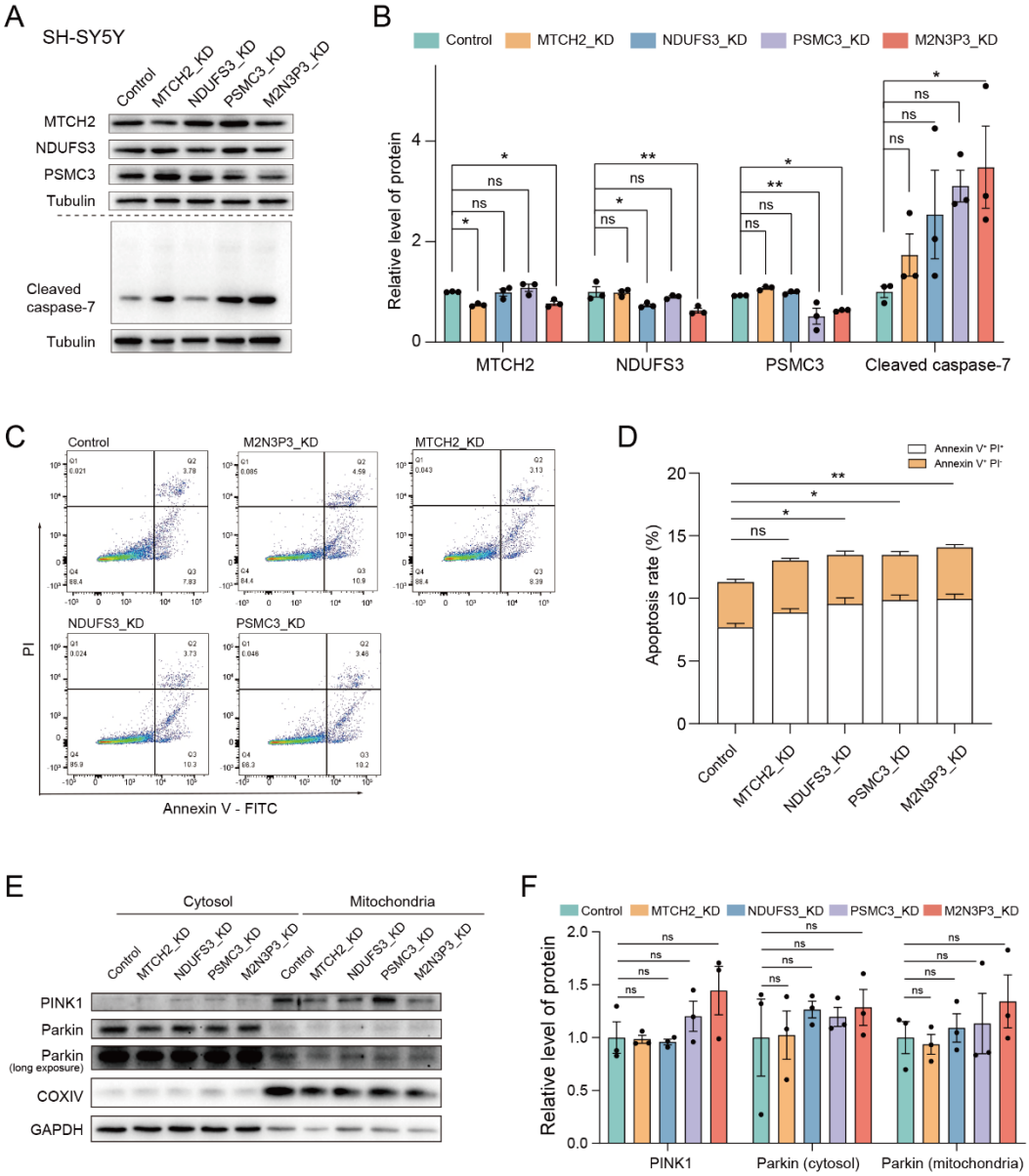

Supplementary Figure 6. Synergistic induction of apoptosis by combined knockdown of *MTCH2*, *NDUFS3*, and *PSMC3* in SH-SY5Y cells.

(A-B) Protein expression levels of caspase-7, MTCH2, NDUFS3, and PSMC3 in SH-SY5Y cells following individual knockdown of *MTCH2*, *NDUFS3*, and *PSMC3* or triple gene knockdown (M2N3P3_KD) (A). (B) Quantitation of protein levels in (A) (n = 3 per group).

(C) Flow cytometry of SH-SY5Y cells following individual knockdown of *MTCH2* (MTCH2_KD), *NDUFS3* (NDUFS3_KD), and *PSMC3* (PSMC3_KD), and triple gene knockdown (M2N3P3_KD). Cells were double-stained with Annexin V and propidium iodide (PI). Cells underwent early and late stages of apoptosis were defined as Annexin V^+ PI^- and Annexin V^+ PI^+, respectively.

(D) Percentage of cells with apoptosis in (C) (n = 8 per group).

(E-F) Protein levels of PINK1, Parkin, COX-IV, and GAPDH in mitochondrial and

cytosolic fractions of U251-APP cells following individual gene knockdown (*MTCH2* knockdown, MTCH2_KD; *NDUFS3* knockdown, NDUFS3_KD; *PSMC3* knockdown, PSMC3_KD) or triple gene knockdown (M2N3P3) (**E**). (**F**) Quantitation of protein levels in (**E**) ($n = 3$ per group).
Data in (B, D and F) are presented as mean ± SD, quantified by one-way ANOVA; ns, not significant; *, $P < 0.05$; **, $P < 0.01$.

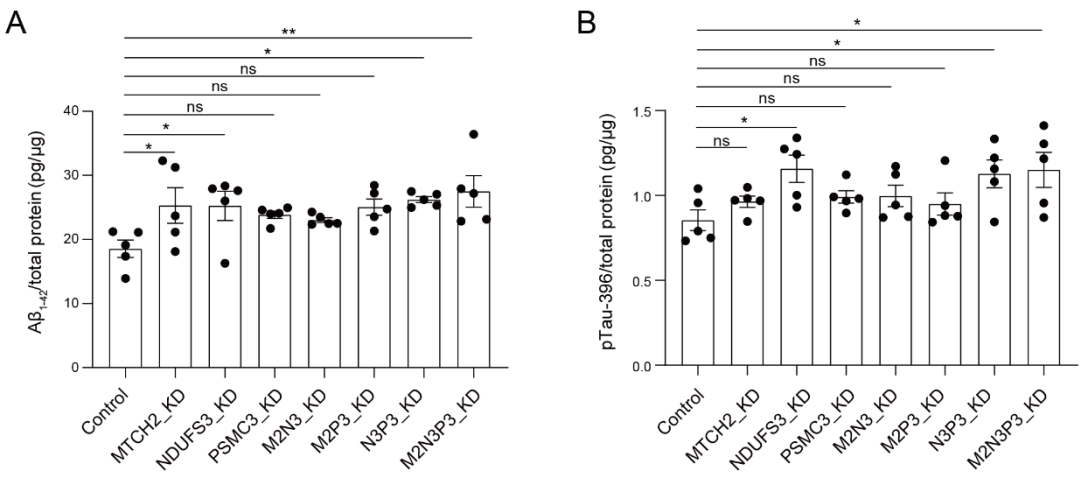

Supplementary Figure 7. Modulation of Aβ$_{1-42}$ and pTau-396 by individual, pairwise, and triple knockdown of *MTCH2*, *NDUFS3*, and *PSMC3* in U251-APP cells.

(A-B) Levels of Aβ$_{1-42}$ in culture supernatants (A) and pTau-396 in cell lysates (B) of U251-APP cells following individual knockdown of *MTCH2* (MTCH2_KD), *NDUFS3* (NDUFS3_KD), and *PSMC3* (PSMC3_KD), pairwise knockdown of *MTCH2* + *NDUFS3* (M2N3_KD), *MTCH2* + *PSMC3* (M2P3_KD), or *NDUFS3* + *PSMC3* (N3P3_KD), and triple gene knockdown (M2N3P3_KD). Aβ$_{1-42}$ and pTau-396 levels were measured by ELISA (n = 5 per group).

Data in (A and B) are presented as mean ± SD, quantified by one-way ANOVA; ns, not significant; *, $P < 0.05$; **, $P < 0.01$.

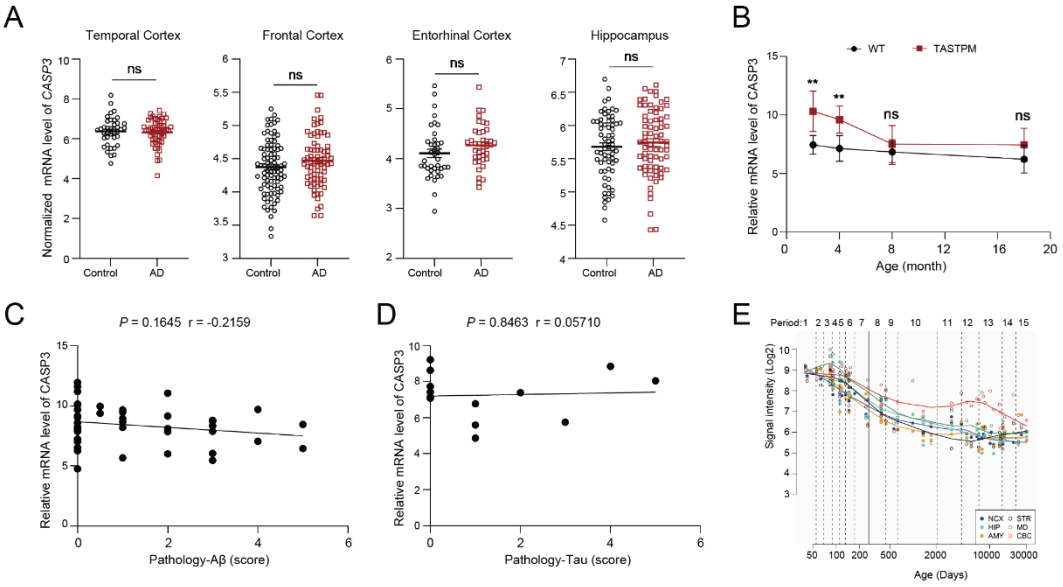

Supplementary Figure 8. Alterations in *CASP3* mRNA levels in brain tissues of AD patients and AD mice.

(A) mRNA expression levels of *CASP3* in the entorhinal cortex, frontal cortex, temporal cortex, and hippocampus of AD patients (AD) and controls (Control) based on compiled datasets [6]. Values are presented as mean ± SD, quantified by two-tailed unpaired *t*-test; ns, not significant.

(B) mRNA expression level of *Casp3* in brain tissues from WT and homozygous TASTPM mice (homozygous $APP^{k670N/M671L}$ and $PSEN1^{M146V}$ mutations) at different ages (2 months, WT, $n = 8$, TASTPM, $n = 4$; 4 months, WT, $n = 7$, TASTPM, $n = 4$; 8 months, WT, $n = 8$, TASTPM, $n = 4$; 18 months, WT, $n = 7$, TASTPM, $n = 2$), based on MouseAC dataset [2]. Values are presented as mean ± SD, quantified by two-way ANOVA with Sidak's multiple comparisons test; ns, not significant; **, $P < 0.01$.

(C-D) Correlation between *Casp3* mRNA expression and Aβ pathology (C) and between *Casp3* mRNA expression and Tau pathology (D) in AD mice. Original data for *Casp3* mRNA expression and Aβ pathology of APP mutant mice (13 homozygous $APP^{k670N/M671L}$, 14 homozygous $APP^{k670N/M671L}$-$PSEN1^{M146V}$, and 16 heterozygous $APP^{k670N/M671L}$-$PSEN1^{M146V}$ mutant mice) and for *Casp3* mRNA expression and Tau pathology (14 $MAPT^{P301L}$ mutant mice) were retrieved from the MouseAC dataset [2]. Pearson's correlation test was used for statistical analysis.

(E) *CASP3* mRNA expression pattern during development and aging in human brain based on the HBT dataset [7].

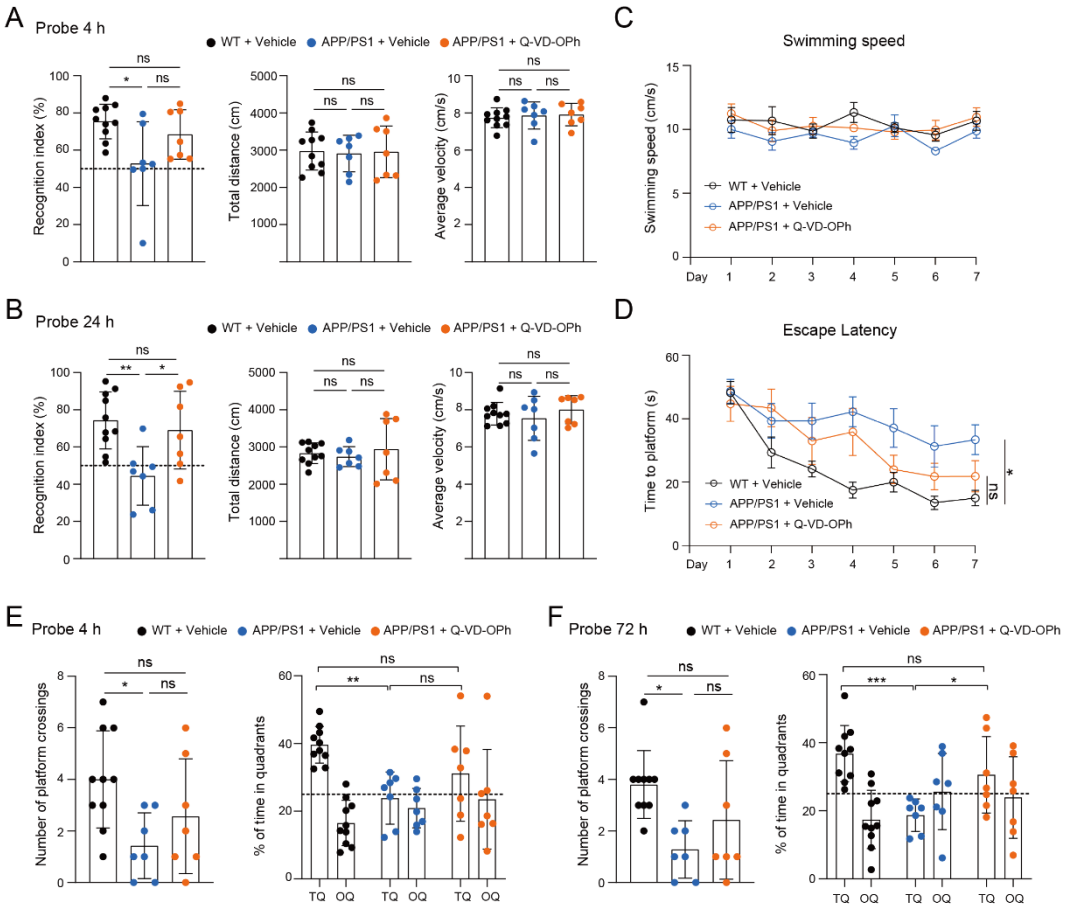

Supplementary Figure 9. Behavioral assessments following 3 months of Q-VD-OPh treatment.

(A-B) Recognition index, total distance, and average velocity recorded during novel object recognition test at the 4-h (A) and 24-h (B) probe trials (WT mice + vehicle, n = 10; APP/PS1 + vehicle, n = 7; APP/PS1 + Q-VD-OPh, n = 7). Data are presented as mean ± SD, quantified by one-way ANOVA, ns, not significant; *, $P < 0.05$, and **, $P < 0.01$.

(C-D) Swimming speed (C) and escape latency (D) measured during training phase of the Morris water maze test in the same cohort as (A). Data are presented as mean ± standard error of the mean (SEM), quantified by two-way ANOVA, ns, not significant; *, $P < 0.05$.

(E-F) Number of target platform crossings and time spent in target quadrant during the 4-h (E) and 72-h (F) probe trials. TQ, target quadrant; OQ, opposite quadrant. Data are presented as mean ± SD, quantified by one-way ANOVA, ns, not significant; *, $P < 0.05$, **, $P < 0.01$, ***, $P < 0.001$.

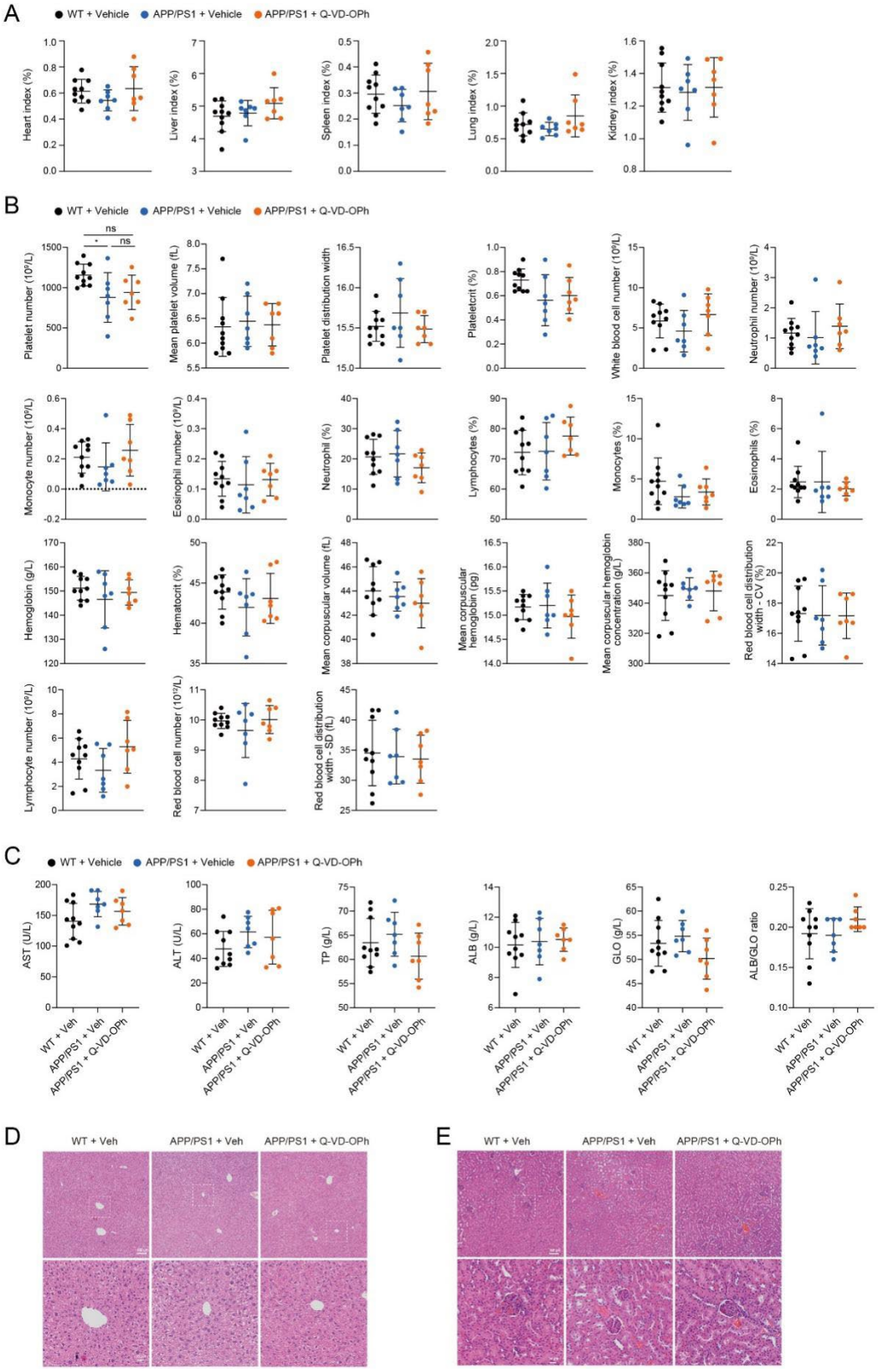

Supplementary Figure 10. Routine blood examination and biochemical indicator detection in APP/PS1 mice after Q-VD-OPh administration.

(A) Weights of heart, liver, spleen, lung, and kidney of WT and APP/PS1 mice with or

without Q-VD-OPh administration (WT + vehicle, $n = 10$; APP/PS1 + vehicle, $n = 7$; APP/PS1 + Q-VD-OPh, $n = 7$). Organ index, organ/body weight ratio.
(B) Routine blood examination of mice described in (A).
(C) Serum aspartate aminotransferase (AST), alanine aminotransferase (ALT), total protein (TP), albumin (ALB), and globulin (GLO) levels in mice described in (A).
(D-E) Histological analysis of liver and kidney tissues in WT and APP/PS1 mice with or without Q-VD-OPh administration.
Data are presented as mean ± SD, quantified by one-way ANOVA (A, B, C), ns, not significant; *, $P < 0.05$, and **, $P < 0.01$.

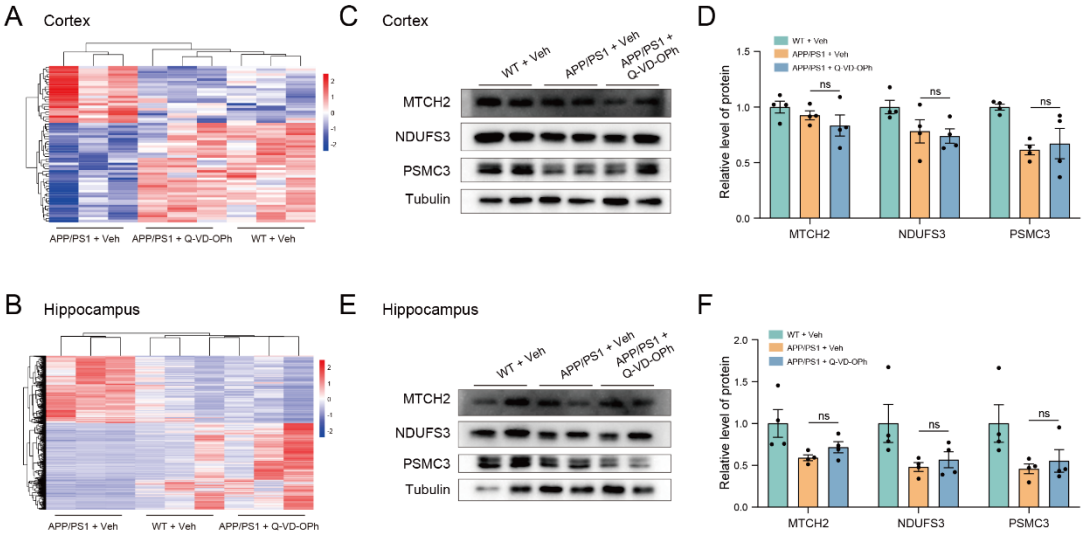

Supplementary Figure 11. Additional RNA-seq analysis and Western blotting of hippocampus and cortex tissues from wild-type (WT) and APP/PS1 mice with or without Q-VD-OPh administration.

(A-B) RNA-seq heatmap of cortex (A) and hippocampus (B) in WT and APP/PS1 mice with or without Q-VD-OPh administration (n = 3 per group).

(C-D) Western blotting for MTCH2, NDUFS3, and PSMC3 proteins in the cortex tissues of WT and APP/PS1 mice with or without Q-VD-OPh administration (C). Protein quantification was performed in four mice per group (WT + Vehicle (Veh), APP/PS1 + Vehicle (Veh), APP/PS1 (AD) + Q-VD-OPh) (D).

(E-F) Western blotting for MTCH2, NDUFS3, and PSMC3 proteins in the hippocampus tissues of WT and APP/PS1 mice with or without Q-VD-OPh administration (E). (F) Quantification of protein levels in (E).

Values are presented as mean ± SD in (D and F). Statistical analyses were conducted one-way ANOVA (D and F); ns, not significant.

Supplementary Table S1. Small interfering RNA (siRNA) sequences.

siRNA for gene	siRNA	Sequence (5'-3')
MTCH2	siMTCH2-1	GGCAGAGAATCCAAGTACT
	siMTCH2-2	GGAAGAGGGCATTCTAGGA
	siMTCH2-3	ACGTGAAAGTGCTCATCCA
ACP2	siACP2-1	GTTCACCAGTGAAGACATA
	siACP2-2	GGGTTTGGTCAGTTAACCA
	siACP2-3	GCTATCACGGCTTCCTAAA
NDUFS3	siNDUFS3-1	GGATCCGTGTGAAGACCTA
	siNDUFS3-2	GCCCAAGTATGTCCAACAA
	siNDUFS3-3	GAAAGACTTTCCTCTATCT
PSMC3	siPSMC3-1	GGAGGATGGTGCCAATATT
	siPSMC3-2	CCACGAGGACTACATGGAA
	siPSMC3-3	CAAGTGTGCTGTGATCAAA

Supplementary Table S2. Primer pairs for qRT-PCR analyses of mouse and human genes

Primer pairs	**Sequence (5'-3')**
Mouse	
Forward for *Gapdh*	TGGCCTTCCGTGTTCCTAC
Reverse for *Gapdh*	GAGTTGCTGTTGAAGTCGCA
Forward for *Mtch2*	TGGGCGACAAGTATGTCAGC
Reverse for *Mtch2*	AGGACTCCTGAACACAGTCTT
Forward for *Ndufs3*	CTGTGGCAGCACGTAAGAAG
Reverse for *Ndufs3*	GCTTGTGGGTCACATCACTCC
Forward for *Psmc3*	GACCGTGTGGGATGAAGCTG
Reverse for *Psmc3*	CGCTGGACAATCTCTTCCGTG
Forward for *Acp2*	CTGATCCCAACCAAGCCTGA
Reverse for *Acp2*	TATGTAAACCAGGGCAGCCAG
Forward for *C1qtnf4*	TGCAGGCCATGATTTACGAC
Reverse for *C1qtnf4*	CCATCGTGATCGTGGCTAAGTA
Forward for *Actb*	TGAGCTGCGTTTTACACCCT
Reverse for *Actb*	GCCTTCACCGTTCCAGTTTT
Forward for *Madd*	TTCCGGAGAGACCCTTGGAG
Reverse for *Madd*	GGCGCTTGTAGCAGAATTGG
Human	
Forward for *GAPDH*	GACAGTCAGCCGCATCTTCT
Reverse for *GAPDH*	GCGCCCAATACGACCAAATC
Forward for *CASP7*	CGGTCCTCGTTTGTACCGTC
Reverse for *CASP7*	CGCCCATACCTGTCACTTTATCA

Supplementary References

1. Mathys H, Peng Z, Boix CA, Victor MB, Leary N, Babu S *et al*. Single-cell atlas reveals correlates of high cognitive function, dementia, and resilience to Alzheimer's disease pathology. *Cell.* 2023; **186**(20):4365-4385.e4327.
2. Matarin M, Salih Dervis A, Yasvoina M, Cummings Damian M, Guelfi S, Liu W *et al*. A genome-wide gene-expression analysis and database in transgenic mice during development of amyloid or tau pathology. *Cell Rep.* 2015; **10**(4):633-644.
3. Song M, Yang X, Ren X, Maliskova L, Li B, Jones IR *et al*. Mapping cis-regulatory chromatin contacts in neural cells links neuropsychiatric disorder risk variants to target genes. *Nat Genet.* 2019; **51**(8):1252-1262.
4. Nott A, Holtman IR, Coufal NG, Schlachetzki JCM, Yu M, Hu R *et al*. Brain cell type-specific enhancer-promoter interactome maps and disease-risk association. *Science.* 2019; **366**(6469):1134-1139.
5. Schrode N, Seah C, Deans PJM, Hoffman G, Brennand KJ. Analysis framework and experimental design for evaluating synergy-driving gene expression. *Nat Protoc.* 2021; **16**(2):812-840.
6. Xu M, Zhang DF, Luo R, Wu Y, Zhou H, Kong LL *et al*. A systematic integrated analysis of brain expression profiles reveals YAP1 and other prioritized hub genes as important upstream regulators in Alzheimer's disease. *Alzheimers Dement.* 2017; **14**(2):215-229.
7. Kang HJ, Kawasawa YI, Cheng F, Zhu Y, Xu X, Li M *et al*. Spatio-temporal transcriptome of the human brain. *Nature.* 2011; **478**(7370):483-489.